



POLITECNICO DI TORINO

Master of Science in Energy and Nuclear Engineering

Master Thesis

**Measurement of the Thermal Dissociation Rate
Constant of CF_3I to $CF_3 + I$ Using Laser
Absorption Spectroscopy in a High Repetition Rate
Shock Tube**

Supervisor

prof. Luciano ROLANDO

prof. Patrick LYNCH

Candidate:

Alice MORO

AA 2022/2023

Abstract

Trifluoroiodomethane (CF_3I) has gained attention as a potential fire suppressant due to its low environmental impact. It is considered as an alternative to fire suppressants containing bromine or chlorine, which have been phased out due to their detrimental effects on the ozone layer under the Montreal Protocol, signed in 1987. CF_3I exhibits a low ozone depletion potential and is therefore considered a promising candidate for new fire suppression systems. In the context of utilizing CF_3I in aircraft applications, flammability limits need to be understood. To comprehensively comprehend the flammability limits, a deep understanding of the secondary chemistry associated with CF_3I is imperative. The reactions involved in secondary chemistry contribute to the overall suppression of combustion and the extinguishing of fires. However, in order to delve into the intricacies of secondary chemistry, it is essential to first gain a comprehensive understanding of the primary dissociation channel of CF_3I . This study focuses on investigating the thermal dissociation rate constant of CF_3I to $CF_3 + I$. In order to measure the thermal dissociation rate, the time resolved concentration of I was measured using laser absorption spectroscopy in a shock tube. The experimental measurements encountered challenges due to the low signal strength caused by a short pathlength in the shock tube. Because the absorption of iodine is small and beam steering is large in the shock tube, different methods for ensemble averaging, and using a fixed wavelength double pass were used.

Cantera, a chemical kinetics simulation software, was utilized to compare and validate the experimental results with models based on the rate constant values found in literature.

The data were analyzed averaging experiments with similar characteristics temperatures, in order to overcome deviations that vary for every experiments, due to a low signal problem. The

simulation and the experimental results were compared and the rate constant was found through a fitting process.

Ethyl iodide (C_2H_5I) was also studied and used as a benchmark due to its well-known rate constant of thermal dissociation to $C_2H_5 + I$, to validate the experimental and analytical approach. Subsequently, the study was extended to CF_3I , as the rate constant of the initial dissociation is not certain. The temperature range for the experiments was between 1000-1500 K and a pressure of 3 bar, using a 2% composition for CF_3I mixture with argon. The obtained rate constant for CF_3I thermal dissociation to $CF_3 + I$ is $k(T) = 10^{14.61} \cdot T^{-0.47} \cdot \exp\left(-\frac{11132}{T}\right)$ [s^{-1}].

The developed method enables accurate prediction of rate constants, facilitating the evaluation and application of CF_3I as a fire suppressant.

Acknowledgments

I would like to express my heartfelt gratitude to my supervisors, Patrick Lynch and Luciano Rolando, for their guidance, support, and expertise throughout this research journey.

To my esteemed colleagues Rizwan, Ashish, Anand, Abhinav, Matt, Matthew, Mukul, Dev, and Mark, I extend a special thank you for your tremendous support in completing this thesis. I could have never done this without your collaboration and willingness to always lend a helping hand.

I would also like to express my heartfelt appreciation to my friends: the bonds we have forged over the years, whether in Chicago, Torino, or Verona, have been an invaluable source of inspiration and encouragement. Your support, shared laughter, and cherished memories have made this journey all the more meaningful and enjoyable. In particular, I want to extend my sincere thanks to Giuditta, Clarissa, Elisa, Giulia, Martina, Chiara, Silvia, Adriana, Francesco, Pierfrancesco, and Marco for their help and support, even during the most challenging times.

To my family, I want to express my gratitude for your boundless love, understanding, and constant motivation. Your belief in my abilities has been the driving force behind my achievements. Thank you for always being there, supporting me unconditionally, and empowering me to pursue my dreams. Your strength, dedication, and guidance serve as an inspiration and I aspire to emulate these qualities in both my personal and professional life.

Lastly, I want to extend my deepest appreciation to everyone who has played a role in the completion of this thesis and contributed to my personal growth. Your support has been invaluable on this journey.

Table of Contents

<i>1. Introduction</i>	1
1.1 Motivation.....	1
1.2 Uncertainty in rate constant values.....	4
1.3 Thesis outline	7
<i>2. Theory</i>	9
2.1 Chemical kinetics introduction.....	9
2.2 Cantera model	13
<i>3. Experimental Setup</i>	20
3.1 High Repetition Rate Shock tube at UIC.....	20
3.2 Mixture preparation.....	28
3.3 Laser absorption setup.....	30
3.4 Diagnostic technique: laser absorption spectroscopy	34
3.5 Beam steering and handling low absorbances	38
<i>4. Modelling</i>	41
4.1 Processing technique	41
4.2 Prediction method	50
<i>5. Experiments and results</i>	53
5.1 Experiments conducted	53
5.2 Evaluation of the three laser configurations	54
5.3 <i>C₂H₅I</i> experiments	56
5.4 <i>CF₃I</i> experiments.....	64
<i>6. Conclusions and Recommendations for Future Work</i>	73
<i>References</i>	75

Table of Figures

Figure 1: <i>CF3I</i> thermal dissociation first order rate constant for different studies [6].....	6
Figure 2: Activation energy chart.	10
Figure 3: Reaction rate sensitivity to I concentration. Initial conditions: T=1250 K, P=3 bar, <i>CF3I</i> =20000ppm, at 0.3 ms.	18
Figure 4: Reaction rate sensitivity to I concentration. Initial conditions: T=1250 K, P=3 bar, <i>C2H5I</i> =10000 ppm, at 0.3 ms.....	20
Figure 5: x-t diagram for a shock tube.....	22
Figure 6: Schematics of the miniature HRRST at UIC.....	24
Figure 7: Sampling line process flow diagram.	29
Figure 8: Concentration in ppm from GC.....	30
Figure 9: Schematics of the laser absorption diagnostic setup for fixed wavelength single pass experiments.	32
Figure 10: Schematics of the laser absorption diagnostic setup for fixed wavelength double pass experiments.	33
Figure 11: Final setup double pass experiments.	34
Figure 12: Absorption cross section of iodine at a central wavenumber of 7603.1384 cm^{-1} . ..	37
Figure 13: Signal of an individual double pass experiment.....	39
Figure 14: Average intensity detected on 100 non-resonant experiments.	40
Figure 15: Signal intensity for an individual experiment.	41
Figure 16: Comparison between the absorption signal of a single experiment and a group of binned experiments.	43

Figure 17: Shock velocities within two different groups: group 1 (low temperature) and group 10 (high temperature).....	44
Figure 18: Pressure profiles within two different groups: group 1 (low temperature) and group 10 (high temperature).....	45
Figure 19: Shocks distribution for each group and its temperature range in <i>CF3I</i> experiments.	46
Figure 20: Pressure profiles from a single pass experiment (orange curve) and from the average of one set of double pass experiments (blue curve).....	48
Figure 21: Absorption curve for one set of <i>CF3I</i> experiments. The yellow dot SB stands for stagnation bubble point and RW stands for reflected waves point, after which this phenomenon becomes more relevant.	49
Figure 22: Schematics of the analysis technique.	52
Figure 23: Comparison between a single pass and a double pass experiment at 1% <i>C2H5I</i> , T=1, 1293 K.....	55
Figure 24: Comparison of simulation and experimental curves for two distinct shock groups representing different temperature ranges, with error bars indicating experimental uncertainties.	57
Figure 25: Curve fitting analysis for two temperature ranges (1137-1198 K on top and 1401-1495 K on bottom) focusing on the period from stagnation bubble formation to reflected wave arrival.	59
Figure 26: Comparison of three experiments, two ran on the first day and one on the third, with 1% <i>C2H5I</i> at T=1375 K.	61
Figure 27: Shocks distribution for each group and its temperature range in <i>C2H5I</i> experiments from one day.	62

Figure 28: Arrhenius plot comparing experimentally determined rate constant (blue line) with the uncertainty limits (black dashed lines) and the rate constant from the mechanism file (red line) for <i>C2H5I</i> experiments.....	63
Figure 29: Difference between the agreement between experimental values and simulation curve using the rate constant provided by Cobos et al. [10] (top) and the one by Bystrov et al. [9] (bottom) for one binned group of experiments.	65
Figure 30: Curve fitting analysis stagnation bubble to rarefaction wave for a low temperature range group of experiments (top) and a high one (bottom).	67
Figure 31: Comparison between different fittings with different coefficients to which the rate constant is multiplied: 0.7, 0.9 (best), 1.3.	69
Figure 32: Arrhenius plot comparing experimentally determined rate constant (blue line) with the rate constant from the mechanism file (red dashed line) for <i>CF3I</i> experiments.	70
Figure 33: <i>CF3I</i> thermal dissociation rate constant for different studies and compared to this work.	71
Figure 34: Comparison between first order rate constants and high-pressure limit by Bystrov et al. [9].	72

Table of Tables

Table 1: Relevant reactions in the early stages of decomposition of <i>CF3I</i>	5
Table 2: Relevant reactions in the early stages of <i>CF3I</i> thermal dissociation mechanism.	17
Table 3: Relevant reactions in the early stages of <i>C2H5I</i> thermal dissociation mechanism.	19
Table 4: Values for the evaluation of the iodine spectrum from [22].	37

Table 5: Experiments run.....	53
Table 6: Relevant reactions in the early stages of <i>CF3I</i> thermal dissociation mechanism.	66

1. Introduction

1.1 Motivation

Fire suppression systems ensure the safety and protection of aircraft and their occupants. In the aviation industry, the risk of fire poses a significant threat that must be effectively managed. Aircrafts are susceptible to fire incidents because of their various fuel sources, electrical systems, and other potentially flammable components. Therefore, the implementation of robust and efficient fire suppression systems is essential to minimize the potential for catastrophic events and ensure the safety of passengers and crew members.

The objective of fire suppression systems in aircraft is to detect, control, and extinguish fires promptly, preventing their spread and reducing potential damage.

Fire incidents can occur during flight or on the ground and having reliable and efficient fire suppression systems ensures that fires can be quickly contained, allowing for safe evacuation of passengers and crew, minimizing the risk of injury or loss of life.

Efficient chemical inhibition and suppression of flames occur through the reduction of flame propagating radicals (H, O, and OH) towards their equilibrium concentrations. This reduction can be achieved by two mechanisms. Firstly, the inhibitor breakdown products react with radicals, forming stable and inert product species within the flame. Secondly, catalytic radical recombination takes place, where intermediate species formed from the breakdown products of the inhibitor facilitate the formation of more stable molecules through a gas phase catalytic cycle. For an inhibitor to be effective, it needs to meet certain criteria. Firstly, it should break down in the flame with a relatively low activation energy, allowing the proper intermediates for the catalytic cycle to be present and interact with the radical pool for an adequate duration. Furthermore, the

catalytic inhibitor should generate intermediates that can regenerate themselves in the catalytic cycle, undergoing fast and nearly thermally neutral reactions. Additionally, the breakdown of the inhibitor should result in intermediate species that can reach the appropriate region of the flame where peak chain branching reactions occur, corresponding to the location of peak radical volume fractions [1]. The rate constant serves as a fundamental parameter that quantifies the speed at which the suppressant dissociates and reacts with fire-extinguishable radicals.

Various fire suppression technologies and agents have been developed to combat aircraft fires effectively. Halon 1301, a highly efficient fire suppressant, gained significant recognition for its remarkable ability to extinguish fires quickly and effectively. Its advantages, including the minimal quantity required, non-destructive deployment, and ability to suppress fires before significant damage occurred, led to widespread installation of Halon 1301 systems in various applications. By the 1980s, these systems were commonly found in computer rooms, commercial and military aircraft, and numerous museums, safeguarding valuable contents, and optimizing storage space [1].

In 1985, the discovery of the Antarctic ozone hole highlighted the need to address ozone depletion. The ozone layer protects life on Earth by absorbing most of the sun's ultraviolet (UV) radiation. However, the excessive release of ozone-depleting substances (ODS) into the atmosphere was gradually eroding this protective layer. As a response to this alarming situation, the international community came together to negotiate the Montreal Protocol on Substances that Deplete the Ozone Layer. Signed in 1987, the protocol represented a global commitment to phase out the production and consumption of ODS. This agreement was a landmark international environmental agreement: it was signed by all the 197 countries of the United Nations and, along with its parent treaty,

the Vienna Convention for the Protection of the Ozone Layer, was the first international agreement to ever achieve this distinction [2]. Many chemicals which were commonly used in refrigeration, air conditioning, and fire suppression systems were found to have harmful effects on the ozone layer and were therefore regulated by the treaty, and Halon 1301 (CF_3Br) was one such chemical. The Ozone Depletion Potential (ODP) is a metric used to measure the ability of a substance to destroy ozone molecules relative to chlorofluorocarbon-11 (CFC-11), which is assigned an ODP of 1. Halon 1301 possesses an ODP of 15.9, which is the highest value among hydrocarbons [3]. This high ODP, coupled with its long atmospheric lifetime of approximately 77.3 years [4], made Halon 1301 a significant contributor to ozone depletion. Additionally, Halon 1301 also has a high Global Warming Potential (GWP), which further increases its environmental effects.

Recognizing the need to mitigate the use of Halon 1301 and other ozone-depleting substances, the Montreal Protocol imposed strict controls and eventually led to a complete ban on the production and use of Halon 1301. The ban took effect in 1994, with the aim of phasing out existing systems and encouraging the adoption of alternative fire suppression methods.

The prohibition of Halon 1301 presented a challenge for industries that relied on its fire suppression capabilities, particularly in aircrafts. Fire suppression systems in aircrafts are crucial for safeguarding lives and minimizing property damage in the event of a fire. Therefore, finding suitable alternatives became a priority.

The search for alternative substances focused on identifying chemicals with lower environmental impact while maintaining effective fire suppression capabilities.

For these reasons, trifluoroiodomethane (CF_3I) emerged as a potential candidate. CF_3I offers advantages such as having a low Ozone Depletion Potential (ODP) and Global Warming Potential (GWP): these characteristics make it an interesting option for fire suppression systems.

The exploration of CF_3I as a potential alternative reflects the commitment to finding environmentally friendly substitutes for ozone-depleting substances. The development and adoption of safe and efficient fire suppression technologies are important for safeguarding lives and property while minimizing the impact on the ozone layer and climate change. Knyazkov et al.'s study [5] investigates the influence of trifluoroiodomethane on the flammability limits of dimethyl ether (DME) in air. CF_3I was found to narrow the flammability limits, particularly the upper limit, indicating its potential as an additive for modifying DME's fire safety characteristics. This research highlights the importance of studying specific additives to enhance the safety and performance of fuel-air mixtures. Knowing the rate constant of this reaction enables a comprehensive understanding of the reaction kinetics associated with CF_3I and its role as a fire suppressant.

1.2 Uncertainty in rate constant values

Before CF_3I can be employed as a fire suppressant, it is important to accurately determine its rate constant for thermal dissociation. This knowledge is needed for optimizing the deployment of CF_3I as an effective fire suppression agent. An accurate rate constant determination also enables the comparison and evaluation of CF_3I 's performance against other fire suppressants. By assessing the rate constant within the context of competing fire suppressant options, it becomes possible to make informed decisions regarding the most suitable agent for specific fire suppression applications. The ability to compare rate constants across different fire suppressants facilitates the identification of superior alternatives and the advancement of fire safety technologies.

Furthermore, accurate rate constant data are essential for the development and refinement of predictive models and simulations in fire dynamics. Incorporating reliable rate constant values into

computational models allows for the accurate prediction of CF_3I 's behavior under various fire scenarios. This predictive capability enhances the design and optimization of fire suppression systems, leading to more effective and efficient fire mitigation strategies.

The rate of disappearance of CF_3I is represented by a first-order reaction, shown in Equation 1:



The most relevant reactions to this thermal process are summarized in Table 1.

Table 1: Relevant reactions in the early stages of decomposition of CF_3I .

Number	Reaction
R1	$CF_3I \rightarrow CF_3 + I$
R2	$CF_3 + CF_3 \rightarrow C_2F_6$
R3	$I_2 (+M) \rightarrow 2I (+M)$
R4	$CF_3 + CF_3I \rightarrow C_2F_6 + I$
R5	$I + CF_3I \rightarrow I_2 + CF_3$

Among the reactions presented in Table 1, the focus of this research is on determining the rate constant of reaction (R1). Extensive investigations have been conducted to characterize this reaction, recognizing its importance in comprehending the thermal dissociation process of CF_3I to $CF_3 + I$.

In Figure 1, this reaction's rate constants reported from previous studies are shown.

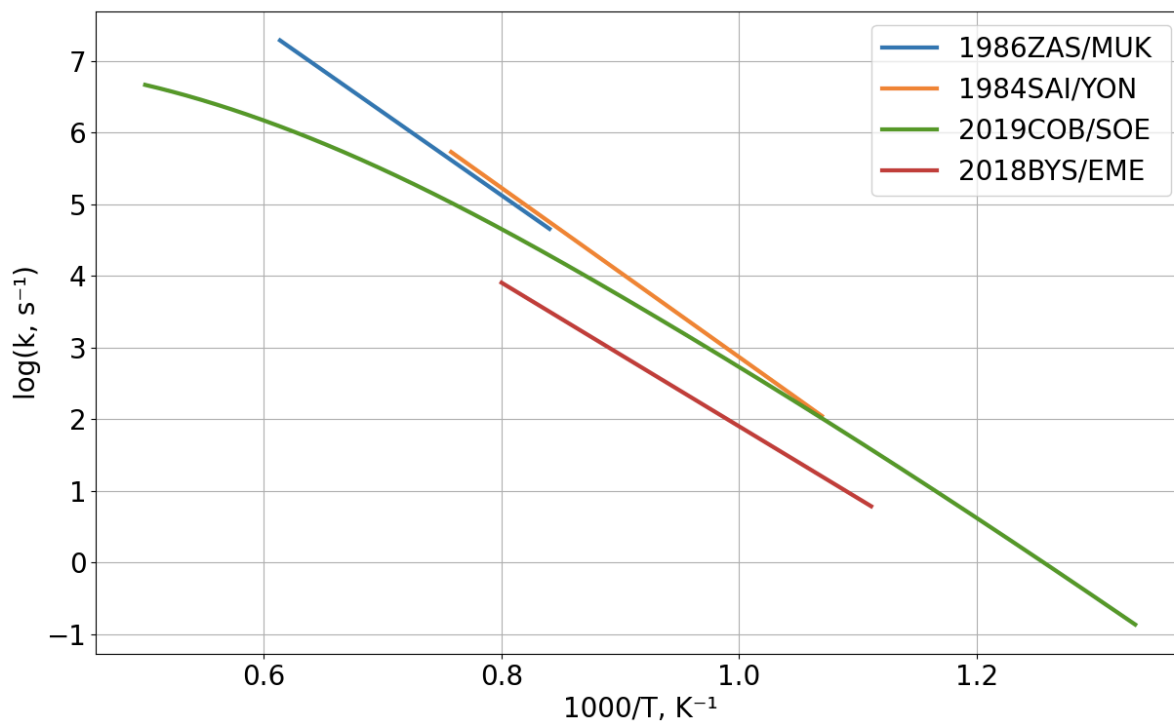


Figure 1: CF_3I thermal dissociation first order rate constant for different studies [6].

In this study, the findings from these prior investigations are utilized to develop a simulation model.

Zaslonko et al. in 1986 [7] and Saito et al. in 1984 [8] measured this reaction's rate constant in shock tube experiments. Zaslonko et al. studied the temperature range from 600 to 1450 K, while Saito et al. studied the temperature range from 935 to 1320 K. Their experimental results are, respectively, shown in curves 1986ZAS/MUK and 1984SAI/YON in Figure 1.

In 2018, Bystrov et al. [9] measured the rate constant for the thermal decomposition of CF_3I reaction in the temperature range from 900 to 1250 K using the shock-tube atomic resonance absorption spectroscopy technique (ARAS). By analyzing the absorption, the authors were able to quantify the concentration of reactive species involved in the decomposition reaction at different

temperatures, allowing to measure the rate constant of this reaction. This is shown in curve 2018BYS/EME in Figure 1.

In 2019, Cobos et al. [10] investigated the reaction kinetics and mechanism of CF_3I decomposition to $CF_3 + I$ using shock tube experiments and advanced theoretical calculations. They specifically studied the falloff behavior of the decomposition reaction in the temperature range from 750 to 2000 K using laser absorption spectroscopy. The paper presents experimental measurements of the rate constant. These measurements are combined with theoretical calculations and modeling to develop a comprehensive understanding of the reaction kinetics. The resulting rate constant is shown in curve 2019COB/SOE in Figure 1.

The data displayed in Figure 1 reveal a significant degree of uncertainty in the rate constant values, as different studies have reported values that vary by more than one order of magnitude. This discrepancy emphasizes the need for further investigation and a comprehensive understanding of the rate constant for thermal dissociation of CF_3I .

1.3 Thesis outline

This research aims to study the reaction rate constant of thermal dissociation of CF_3I through the use of a shock tube. A shock tube provides a controlled and well-defined environment for conducting experiments, being able to generate high-temperature and high-pressure conditions characteristic to combustion. Laser absorption spectroscopy diagnostic technique coupled with the shock tube allows for the precise detection and quantification of reactive species over time, and therefore reveal the speed of the reaction.

The primary objective of this thesis is to explore the thermal dissociation rate constant of CF_3I and devise a methodology for measuring rate constants through the application of laser absorption spectroscopy within a shock tube environment. A specific focus is placed on the scenario in which the signal strength is diminished due to the utilization of a short pathlength, due to the use of the miniature shock tube employed in this study. Therefore, an integral part of this research is to develop a procedure that can effectively measure rate constants despite low signal strength, utilizing different experimental techniques and modelling methods. To achieve this goal, a set of robust processing techniques was developed. Two different systems were used to run experiments: the first system is with ethyl iodide (C_2H_5I) and served as a benchmark with its well-known rate constants, while the second system, with trifluoroiodomethane (CF_3I), aimed to investigate and explore rate constants that were yet to be determined. To ensure the accuracy of the analysis, the C_2H_5I system was initially studied before proceeding with the investigation of CF_3I . This sequential approach allowed for the validation of the experimental methodology and analysis techniques employed. By first examining the C_2H_5I system, any potential errors or uncertainties in the measurements or calculations could be identified and corrected. Once the methodology was confirmed, the investigation of CF_3I was carried out, building upon the knowledge gained from the previous study. The temperature range of 1000 to 1500 K was selected for the experiments due to its ability to encapsulate the behavior and dynamic characteristics of iodine within that specific thermal regime, which is where CF_3I thermal dissociation to $CF_3 + I$ takes place [11]. The pressure at which the experiments were run was 3 bar, which was resulting from shocks in order to cover that specific temperature range.

2. Theory

2.1 Chemical kinetics introduction

In the field of chemical kinetics, the parameter that describes the speed at which a chemical reaction proceeds is called rate constant and it provides quantitative information about the velocity at which reactants are transformed into product. Rate constants are typically represented as $k(T)f(T, P)$, where $k(T)$ represents the temperature-dependent term and $f(T, P)$ represents the pressure-dependent term, representing high temperature fall-off term.

The temperature-dependent term, $k(T)$, quantifies the influence of temperature on the reaction rate.

It is determined by the Arrhenius equation which is shown below in Equation 2:

$$k(T) = A \cdot \exp\left(-\frac{E_a}{R \cdot T}\right), \quad (2)$$

where $k(T)$ is the rate constant, A is the pre-exponential term, which can be temperature dependent, E_a is the activation energy term, R is the universal gas constant, and T is the temperature in Kelvin.

Another form of Arrhenius equation that takes into account the temperature dependence of the A factor is the modified Arrhenius equation, shown in Equation 3.

$$k(T) = A \cdot T^n \cdot \exp\left(-\frac{E_a}{R \cdot T}\right), \quad (3)$$

Where A is the pre-exponential term, which can be temperature dependent, E_a is the activation energy term, R is the universal gas constant, T is the temperature in Kelvin, and the exponent n is

dimensionless and considers the temperature dependence. These values may be different from the ones in Equation 2.

The term A is related to the collisional probability: it takes into consideration the number of collisions that occur per unit time and the fraction of those collisions that have the correct orientation and sufficient energy to lead to a successful reaction.

According to the collisional theory, for a chemical reaction to occur, reactant molecules must collide with sufficient energy to react. This energy barrier is the activation energy E_a , and it is shown in Figure 2.

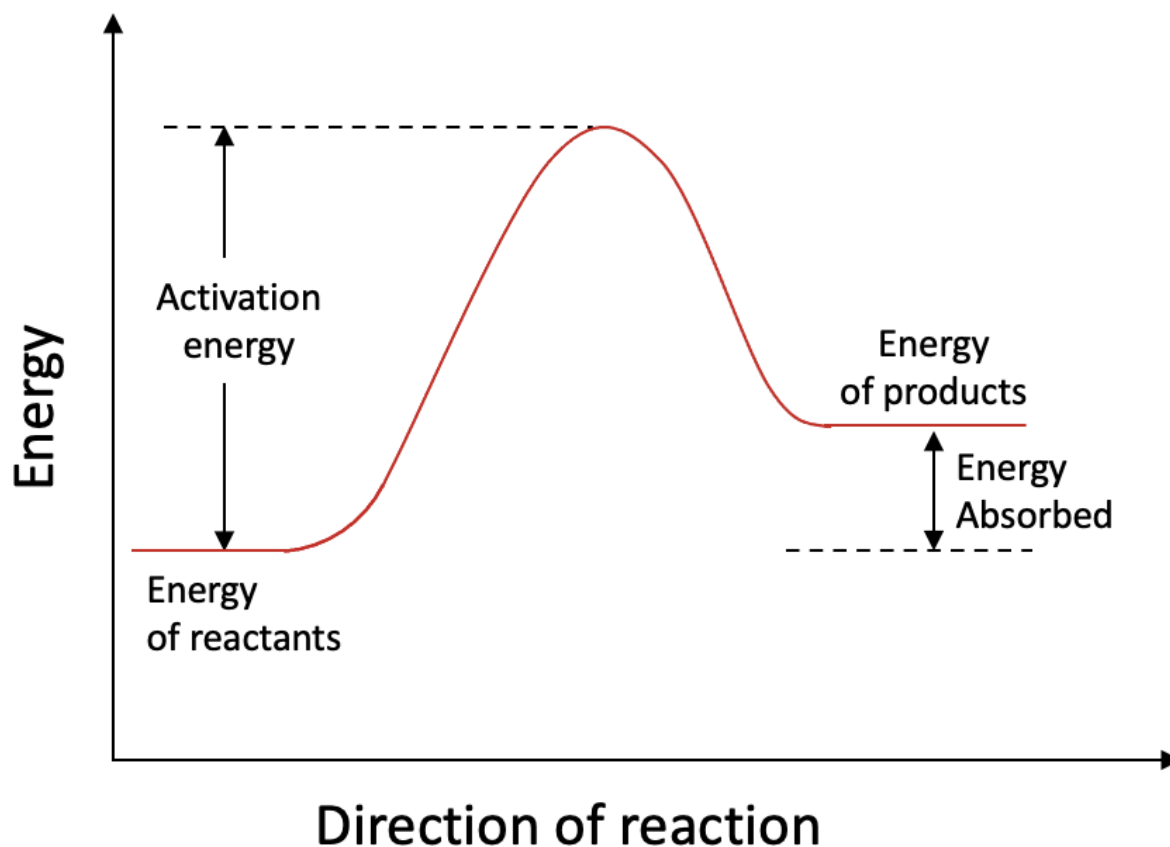


Figure 2: Activation energy chart.

In Figure 2, the vertical axis still represents the energy coordinate, while the horizontal axis represents the reaction coordinate. However, in the case of an endothermic reaction, the energy of the products is higher than the energy of the reactants.

At the beginning of the reaction, the reactants are at a lower energy level. As the reaction progresses, the energy level increases. The energy continues to rise until it reaches the highest point on the curve. It then decreases again until it reaches the value of energy of products.

The activation energy for an endothermic reaction is still represented as the vertical distance between the reactants' energy level and the peak of the curve. This peak represents the transition state, where the reactants are in an intermediate configuration before converting into products.

Reactant molecules with energy equal to or greater than the activation energy can overcome the energy barrier. If these collisions possess sufficient energy to break existing bonds and form new bonds, they result in the formation of products. Molecular structure determines the activation energy. Two factors are related to molecular structure: bond strength and molecular stability. Bond strength within the reactant molecules directly affects the activation energy: weaker bonds are more easily broken, requiring less energy to initiate the reaction while stronger bonds require higher energy input to break, resulting in a higher activation energy. The stability of the reactant molecules and the intermediate species formed during the reaction also impacts the activation energy: more stable molecules and intermediates have lower activation energies because they require less energy to reach the transition state.

The reaction order determines the mathematical form of the rate equation and the corresponding rate constant.

In a first-order reaction, the rate is directly proportional to the concentration of a single reactant. The first-order rate constant represents the proportionality constant in this relationship and is specific to the particular reaction under investigation. The unit of the first-order rate constant is $\left[\frac{1}{s}\right]$.

In contrast, second-order reactions involve the interaction between two reactants. The rate of a second-order reaction is proportional to the product of the concentrations of the reactants or the square of the concentration of a single reactant. The second-order rate constant quantifies the relationship between the reaction rate and the concentrations of the reactants involved. The unit of the second-order rate constant is $\left[\frac{cm^3}{mol \cdot s}\right]$.

This study focuses on the determination of the primary unimolecular rate constant for the thermal dissociation of CF_3I to $CF_3 + I$.

Measuring the rate constant of a particular reaction can be achieved by monitoring the disappearance of reactants or the appearance of products. In cases where the reaction of interest is the dominant or the only significant pathway leading to product formation, tracking the reactants' disappearance or products' appearance provides a direct means of quantifying the reaction rate. By carefully controlling the experimental conditions and employing suitable analytical techniques, such as laser absorption spectroscopy, the progress of the reaction can be precisely monitored, allowing for the measurement of the rate constant and a comprehensive understanding of the reaction kinetics.

A sensitivity analysis was performed to assess the sensitivity of different reaction rates to observables in this system. In a shock tube, this analysis is useful to understand the impact of individual reactions on the kinetics of the system studied. The analysis involves varying the rate coefficients of specific reactions in the chemical mechanism and observing the resulting changes

in the overall reaction kinetics and species concentrations. The calculation of the sensitivity coefficient is also done by Cantera. In this case, the target specie is iodine, so the sensitivity coefficient measures the effect of a parameter change on iodine concentration: if a coefficient is positive, it means that an increase in a reaction leads to an increase in the concentration of iodine, while, if a coefficient is negative, it means that an increase in a reaction leads to a decrease in the concentration of iodine.

2.2 Cantera model

The experimental results were validated by comparing them with a simulation conducted using Cantera [12]. Cantera is an open-source software that can provide a comprehensive set of tools for modeling and simulating chemical kinetics. And thermodynamics in various reactive systems. Cantera enables the simulation of chemical kinetics by solving a system of ordinary differential equations (ODEs) that describe the time evolution of species concentrations based on the reaction rates. After specifying the initial conditions and system properties, Cantera can numerically solve the ODEs to predict the time-dependent behavior of the system. The system properties are specified in the mechanism file, which follows the Chemkin format so that Cantera can interpret the information it contains. The mechanism file describes the chemical system, outlining the elements, molecules, their thermodynamic properties, the reaction equations, and their rate constants.

A fixed-mass, prescribed pressure reactor model is commonly used to simulate and analyze the dynamics of shock tube experiments. This provides a theoretical framework for software tools like Cantera to study the chemical reactions occurring within the shock tube. In this modeling approach, the gas mixture present in the shock tube is represented as a closed system with a fixed

mass. The temperature within the reactor plays a crucial role in governing the reaction kinetics and thermodynamics during the shock tube experiment.

To develop this model, the assumption of ideal gas was made, and equations such as the conservation of mass, energy, and species are considered. These equations are coupled with the equation of state and reaction kinetics to describe the evolution of the gas properties within the reactor. The pressure within the reactor is typically defined as a function of time and adjusted to match the experimental conditions of the shock tube.

To define the model, as described by [13], the conservation of energy equation for a fixed-mass system (Equation 4) is used:

$$\dot{Q} - VdP = m \frac{dh}{dt} \quad (4)$$

In Equation 4, \dot{Q} represents the heat transfer rate, V denotes volume of the system, P is pressure, m is the mass of the system, h is the specific enthalpy, and t represents time. The term dh/dt signifies the time rate of change of the enthalpy of the system. As the system is at a constant volume, \dot{W} is equal to zero.

To define the specific internal energy (u), Equation 5 is introduced:

$$u = \frac{U}{m} = \frac{\sum_{i=1}^N N_i \bar{u}_i}{m} \quad (5)$$

In Equation 5, N_i and \bar{h}_i represent the number of moles and molar enthalpy of species I, respectively.

By differentiating Equation 5, Equation 6 is obtained:

$$\frac{du}{dt} = \frac{1}{m} \left[\sum_i \left(\bar{h}_i \frac{dN_i}{dt} \right) + \sum_i \left(N_i \frac{d\bar{u}_i}{dt} \right) \right] \quad (6)$$

Furthermore, assuming ideal gas behavior, Equation 7 states:

$$\frac{d\bar{u}_i}{dt} = \frac{(\partial \bar{u}_i)}{\partial T} \frac{dT}{dt} = \bar{c}_{v,i} \frac{dT}{dt} \quad (7)$$

In Equation 7, $\bar{c}_{v,i}$ represents the molar specific heat at constant volume of species i.

The molar concentration ($[X_i]$) is defined as the number of species I per unit volume, given by Equation 8, where V denotes the volume of the system.

$$N_i = V [X_i] \quad (8)$$

The rate of change of moles $\left(\frac{dN_i}{dt}\right)$ is related to the rate of reaction ($\dot{\omega}_i$) for species i, as expressed in Equation 9:

$$\frac{dN_i}{dt} = V \dot{\omega}_i \quad (9)$$

where $(\dot{\omega}_i)$ is the species production rate and it represents the change in the number of moles of species i per unit time. Where $\dot{\omega}_i$ is defined as Equation (10):

$$\dot{\omega}_i = \sum_i v_{i,j} q_i, \quad (10)$$

where $v_{i,j}$ is the stoichiometric coefficient and q_i represents the net production rate of species i due to all the reactions in the system. It is the difference between the production rate and consumption rate of species i . This substitution allows for the relationship between the rate of change of moles and the rate of reaction, ultimately deriving the equation for the rate of change of temperature (dT/dt) in terms of heat transfer (\dot{Q}), molar enthalpies (\bar{h}_i), molar concentrations ($[X_i]$), and molar specific heats at constant volume ($\bar{c}_{v,i}$) as shown in Equation 11:

$$\frac{dT}{dt} = \frac{\dot{Q} - \sum_i (\bar{h}_i \dot{\omega}_i)}{\sum_i ([X_i] \bar{c}_{v,i})}. \quad (11)$$

For ideal gases, Equations 12 and 13 define the molar internal energy (\bar{u}_i) and molar specific heat at constant volume ($\bar{c}_{v,i}$), respectively.

$$\bar{u}_i = \bar{h}_i - R_u T \quad (12)$$

$$\bar{c}_{v,i} = \bar{c}_{p,i} - R_u \quad (13)$$

Equation 14 is then transformed into Equation 14 by substituting Equations 6 and 7.

$$\frac{dT}{dt} = \frac{-\sum_i(\bar{h}_i \dot{\omega}_i) + \frac{dP}{dt} + \frac{\dot{Q}}{V}}{\rho \cdot c_{p,i}} \quad (14)$$

The other way that the temperature can change from isentropic pressurization becomes an additional term that goes into Equation 14, expressed as Tao et al. did, using the isentropic assumption in Equation 15.

$$\frac{dT}{dt} = \frac{dP}{dt} \frac{TR_u}{P\bar{c}_p(T)} \quad (15)$$

Where P is pressure and dP/dt is obtained at each time from a polynomial fit from the experimental data.

As for CF_3I system, the mechanism file was written using the reactions and rate constants provided by Papas et al. [11] and the thermal data obtained from Burcat's thermodynamic database [14]. The thermal dissociation rate constant for CF_3I , as utilized by Papas et al., was derived from a study conducted by Cobos et al. [10]. The rate constant for this specific system remains uncertain and is yet to be precisely determined. However, the study by Cobos et al. serves as a valuable reference for comparison purposes in the absence of a definitive rate constant. The rate constants for the most important reactions can be seen in Table 2

Table 2: Relevant reactions in the early stages of CF_3I thermal dissociation mechanism.

	Reaction		A	n	E_a	$\Delta H_{r,298K}$	Ref.
R1	$CF_3I (+M) \rightarrow CF_3 + I (+M)$	k_∞	2.365E22	-2.20	5.749E4	54552	[11]
		k_0	1.300E53	-10.46	6.232E4		
R2	$CF_3 + CF_3 (+M) \rightarrow C_2F_6 + (M)$	k_∞	9.690E10	0.77	0.00	-99359	[11]

		k_0				
		1.491E60	-12.51	5.908E3		
R3	$I + I + M \rightarrow I_2 + M$	2.361E14	0.00	-1.500E3	-36114	[11]
R4	$I + CF_3I \rightarrow I_2 + CF_3$	7.590E12	0.00	1.888E4	18438	[11]

The rate constant is expressed as in Equation 7, and the units of the terms in the table are given in cm^3, mol, s, cal .

where $\Delta H_{r,298K}$ is the standard enthalpy at 298 K. By incorporating the rate constants from Papas et al. and the thermal data from Burcat's thermodynamic database [14], the mechanism file provides a foundation for modeling the CF_3I system on Cantera. After defining the mechanism file, the sensitivity analysis for the system was done, and is shown in Figure 3.

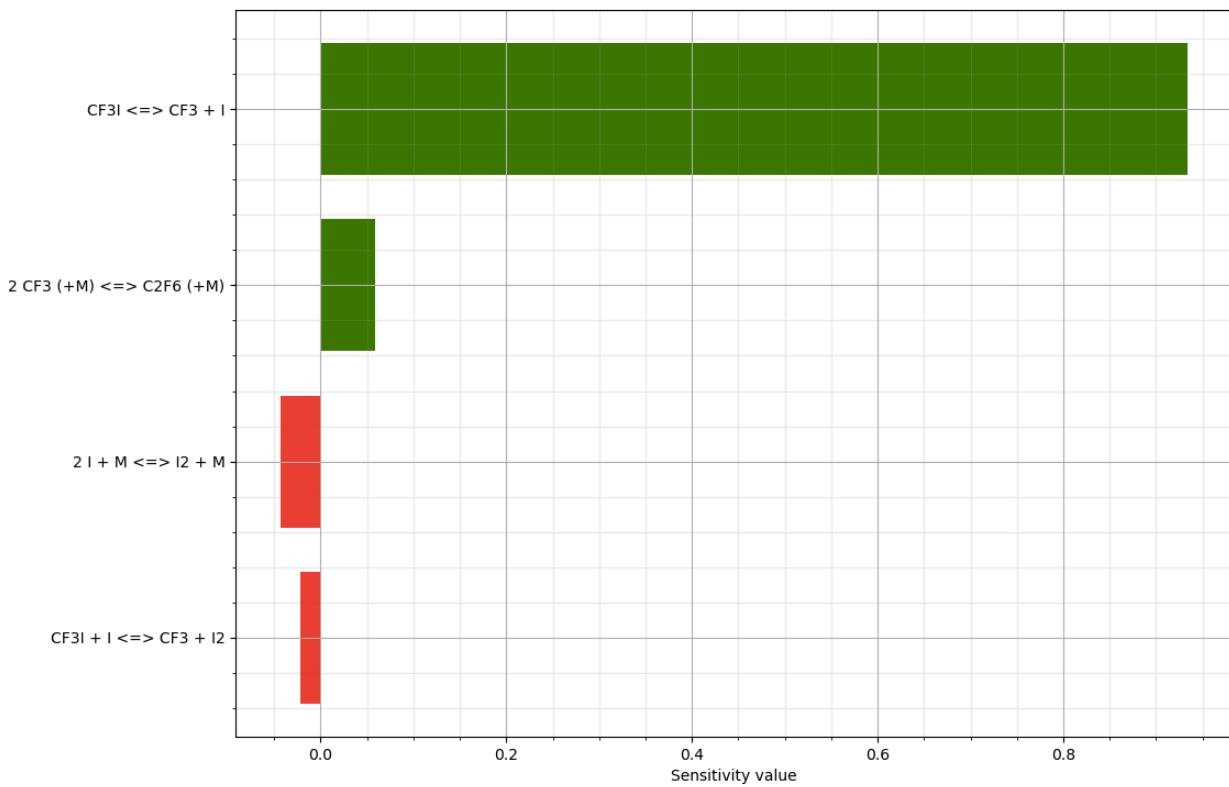


Figure 3: Reaction rate sensitivity to I concentration. Initial conditions: $T=1250$ K, $P=3$ bar, $CF_3I=20000$ ppm, at 0.3 ms.

The analysis highlights the crucial role of the CF_3I to I reaction in the overall dynamics of the system. Additionally, it emphasizes the significance of CF_3 as an intermediate species in the CF_3I

decomposition pathway. Moreover, the sensitivity analysis underscores the importance of iodine recombination reactions in shaping the behavior of the CF_3I system.

As for C_2H_5I system, the Chemkin file was written using the rate constants by Yang et al. [15], Kumaran et al. [16] and Wang et al. [17] and the thermal data from Burcat's thermodynamic database [14].

Table 3: Relevant reactions in the early stages of C_2H_5I thermal dissociation mechanism.

	Reaction	A	n	E_a	$\Delta H_{r,298K}$	Ref.	
R5	$C_2H_5I \rightarrow C_2H_5 + I$	6.340E9	0.00	3.154E4	55809	[16]	
R6	$C_2H_4 + H(+M) \rightarrow C_2H_5 (+M)$	k_∞	7.590E12	0.00	1.888E4	-36041	[17]
		k_0	2.027E39	-6.64	5.769E3		
R7	$C_2H_5I + H \rightarrow C_2H_5 + HI$	8.912E13	0.00	1.000E3	-15461	[15]	
R8	$H_2 + I \rightarrow H + HI$	2.361E14	0.00	-1.500E3	32933	[15]	

The rate constant is expressed as in Equation 7, and the units of the terms in the table are given in cm^3, mol, s, cal .

This system provided a reference point and validation for the experimental setup and measurement techniques, and for this reason both models and experiments were run

Figure 4 below shows the sensitivity analysis performed on C_2H_5I system.

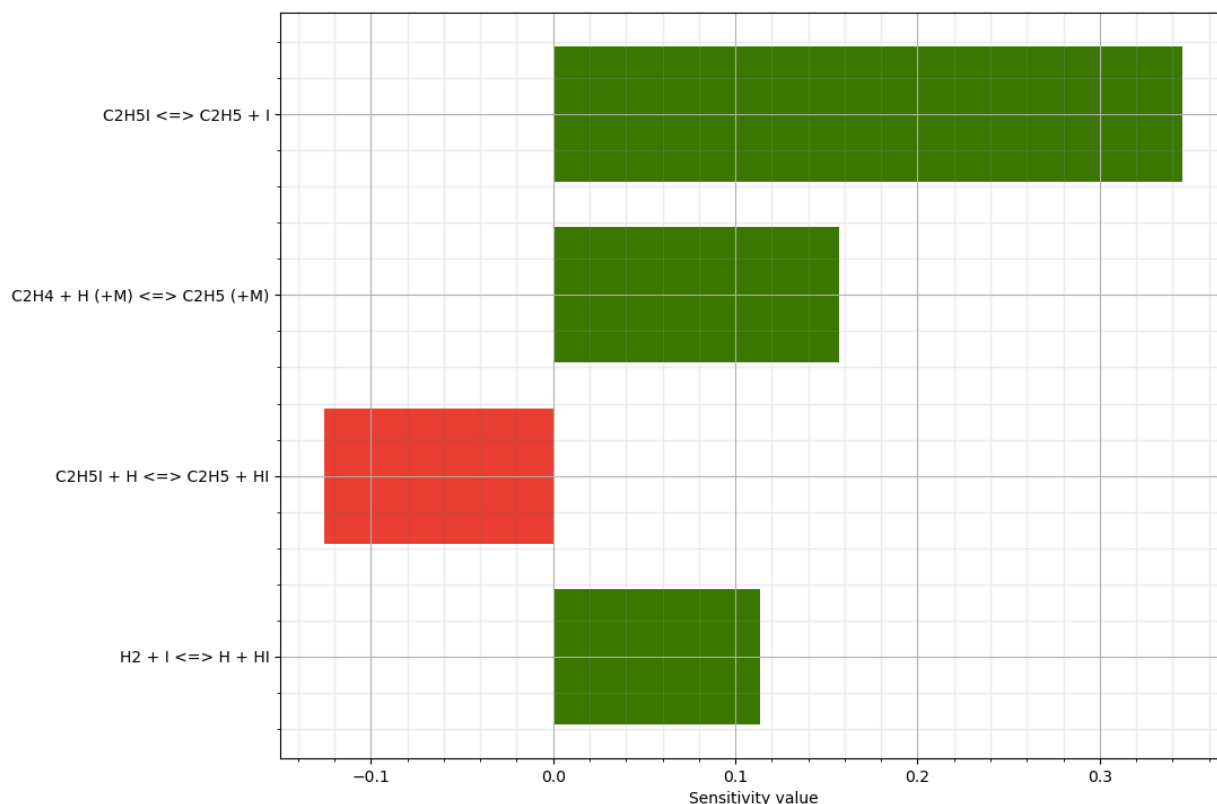


Figure 4: Reaction rate sensitivity to I concentration. Initial conditions: $T=1250\text{ K}$, $P=3\text{ bar}$, $C_2H_5I=10000\text{ ppm}$, at 0.3 ms .

The sensitivity analysis for C_2H_5I system revealed that its thermal dissociation is the most sensitive reaction in determining the overall behavior of the system. However, it is important to note that there are other reactions in the system that also exhibit sensitivity. Therefore, caution must be exercised when interpreting and analyzing the results, taking into account the potential influence of these sensitive reactions on the overall dynamics of the system.

3. Experimental Setup

3.1 High Repetition Rate Shock tube at UIC

A Shock Tube is an experimental apparatus used to study chemical systems, particularly reaction rates and kinetics. It consists of cylindrical tube that is divided into two main sections: the driver

section and the driven section. The driver section is typically filled with a high-pressure gas mixture, such as helium, while the driven section contains a low-pressure test gas of interest.

These two sections are usually separated by a diaphragm, a thin barrier that prevents the gases from mixing initially. When the experiment is initiated, a sudden rupture of the diaphragm occurs, allowing the high-pressure gas from the driver section to rapidly mix with the low-pressure gas in the driven section. This rupture creates a huge pressure differential that creates a shock wave, that propagates down the driven section of the shock tube. Unlike traditional designs that use a diaphragm to separate the driver and driven sections, a fast-acting solenoid-driven high-pressure spring-return valve [18] is utilized in this study. This valve offers several advantages. Firstly, it provides enhanced repeatability since there is no need to replace the diaphragm after each shock. This not only saves time but also ensures consistent performance throughout multiple experiments. Secondly, the solenoid-driven valve offers improved sealing capabilities, minimizing any potential leakage or gas loss during the experimental process. This contributes to the accuracy and reliability of the measurements. Lastly, the high-pressure spring-return valve allows for better throughput rates, enabling faster cycling times and increasing the efficiency of the shock tube system.

As the shock wave travels through the driven section, it compresses the gas and accelerates it towards the endwall. These conditions created by the shock wave closely mimic those encountered in combustion processes. This makes the HRRST an important tool for studying chemical reactions that are relevant to combustion.

In the experimental procedure, the driver section is filled with a high-pressure gas, typically helium, up to a predetermined pressure referred to as P4. On the other hand, the driven section is filled with a mixture of the desired fuel, CF_3I , and an inert gas, such as argon, up to a pressure denoted as P1.

When the solenoid valve opens, it generates an incident shock wave that propagates along the length of the low-pressure section. As the shock wave reaches the end-wall of the driven section, it reflects, causing an increase in pressure and temperature within the tube. The region behind the reflected shock wave, known as region 5. This region is of great interest for studying chemical kinetics and related phenomena. Simultaneously, an expansion wave propagates in the opposite direction towards the high-pressure section. There are two additional regions: region 3 and region 2. Region 2 is the gas between incident shock wave and contact surface which is an imaginary surface that separates driven and driver gases and region 3 is flow behind contact surface.

These regions are shown in the x-t diagram in Figure 5:

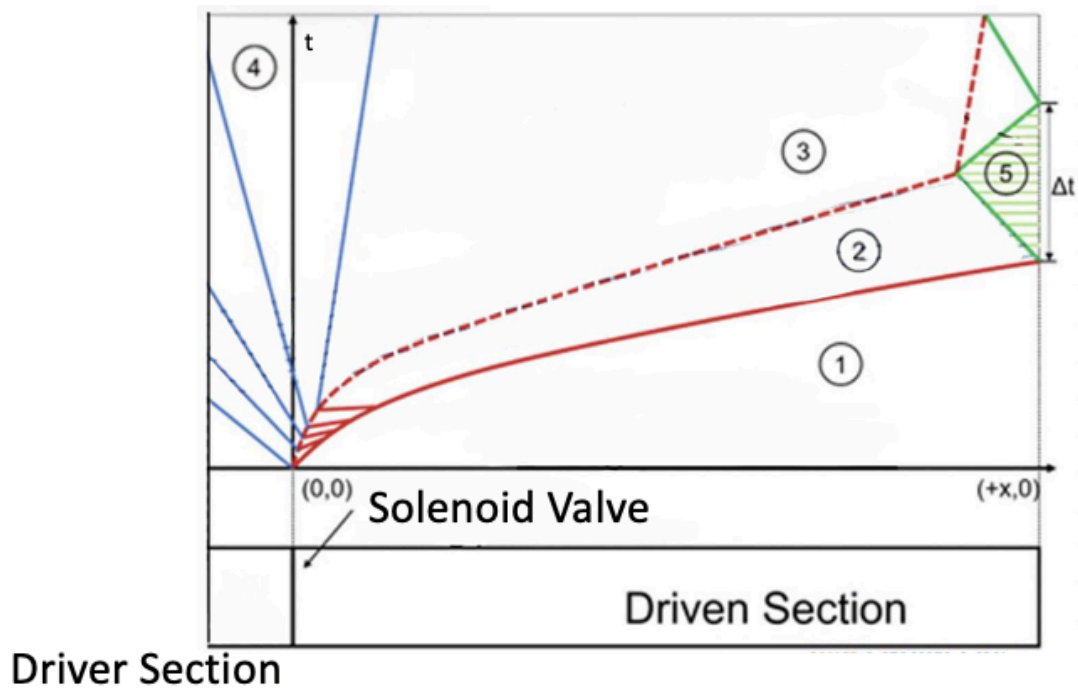


Figure 5: x-t diagram for a shock tube

In Figure 5, the x-axis represents time, usually in microseconds or milliseconds, and the y-axis represents the position along the length of the shock tube. The x-t diagram provides a visual

representation of the shock wave propagation and allows for the analysis of shock wave. The red line represents the incident shock wave, the green line represents the reflected shock wave, and the blue lines represent a rarefaction wave. Δt is the steady time of the reflected shock wave: it represents the time interval between the reflection of the incident shock wave and the reflected waves from the contact surface. [19]

The sudden increase in temperature initiates reactions, allowing to investigate reaction rates, kinetics, and other important aspects of the chemical system under study. By carefully controlling the initial gas conditions, the shock wave parameters, and the diagnostic techniques employed, detailed insights into the reaction mechanisms, energy transfer processes, and species formation pathways can be obtained.

The shock tube operates following a specific cycle. The first step is filling a new charge of the desired gas. This involves introducing the gas into the shock tube to create the desired test condition. Once the shock tube is filled with the test gas, the solenoid valve is actioned. This valve is responsible for initiating the shock wave within the tube. The last step is the purging of the previous test gas. This consists in removing any residual gas or contaminants from the shock tube to prepare it for the next experiment. Purging helps ensure that the test conditions are not influenced by any remnants of previous gases. This is done through the two pneumatic valves shown in Figure 6. Additional details can be found in Ref. [20] and [21].

In this study, the shock tube cycle is performed at a rate of 0.125 Hz. This indicates that each complete cycle, including purging, filling, and firing the driver valve, takes 8 seconds to be completed. This cycle rate determines the frequency at which the experiments are conducted.

The schematics of the miniature HRRST at University of Illinois at Chicago (UIC) is shown in Figure 6.

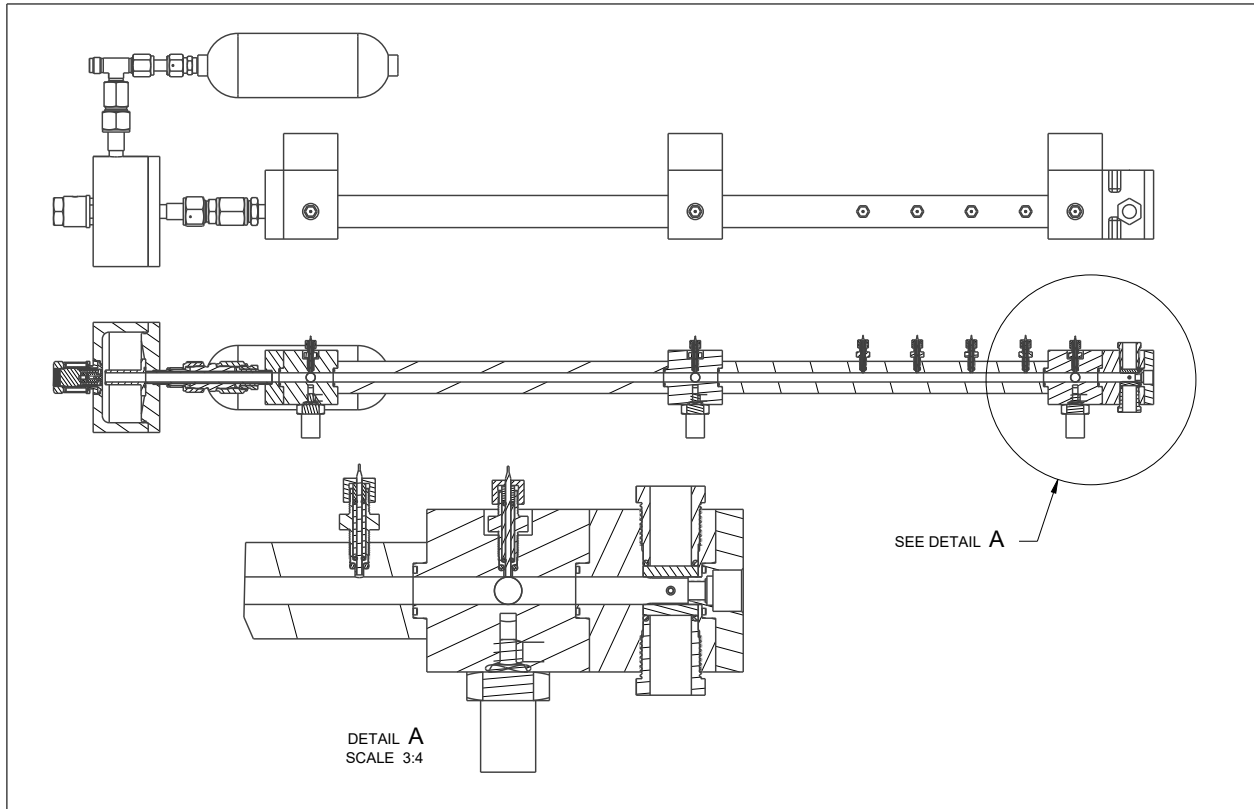


Figure 6: Schematics of the miniature HRRST at UIC.

The experimental setup involves a shock tube with a driver section measuring approximately 1.9 meters in length and a bore width of 12.7 millimeters.

To accurately measure the arrival time and velocity of the incident shock wave, five sidewall-mounted piezoelectric transducers (Dyansesn CA-1135), shown in Figure 6, are strategically placed along the shock tube. These transducers precisely record the time-of-arrival of the shock wave, allowing for the calculation of its velocity. Additionally, a pressure transducer (PCB-105C12) is inserted into the end wall of the driven section. This transducer, positioned along the axis of the shock tube, measures the pressure profile of the reflected shock wave. To allow laser

absorption measurements, which will be described later, two sapphire windows are placed before the end wall. Sapphire is transmissive to the wavelength of laser chosen in this study: this makes it a good choice for the window material.

The shock tube can reach pressures up to 100 bars, and operates at a cycle rate of 4 Hz, providing high-resolution data for the experiments. Advanced diagnostic techniques such as laser absorption spectroscopy are employed. These techniques allow for detailed analysis of gas composition and chemical reactions occurring within the shock tube.

The use of a small diameter and small length in experimental setups can introduce certain drawbacks. One such drawback is the boundary layer effect, which occurs near the walls of the small diameter shock tube. As the gas flows through the narrow tube, a thin layer of gas forms near the walls, known as the boundary layer. Within this layer, the velocity of the gas decreases due to viscous effects, resulting in a slower flow compared to the central region of the tube. This variation in velocity creates gradients in temperature and species concentration, which can deviate from the desired uniform conditions required for accurate measurements [22]. In smaller bore shock tubes, the relative contributions from the boundary layers become more significant compared to larger-scale shock tubes. The reduced size of the tube amplifies the influence of the boundary layers on the flow layer causing the pressure and temperature to rise in the reflected shock region [23].

Additionally, the short test time available in a small length shock tube may not provide sufficient duration for reactions to reach completion or for accurate measurement of reaction rates. This limitation can pose challenges in capturing the complete reaction profile and understanding underlying mechanisms. Furthermore, the small path length restricts the interaction length between

reactants and the shock wave, resulting in lower signal intensities and reduced sensitivity in measuring reaction products or intermediates.

The high repetition rate capability of the HRRST gives a significant advantage: it enables rapid and repeated experiments to be conducted consistently, ensuring the ability to obtain the same experimental conditions repeatedly. This feature also provides a large amount of data in a relatively short amount of time.

A custom software written in LabVIEW handles shock tube operations and data acquisition. For each shock three main parameters can be handled: the driver gas pressure P_4 , the driven gas pressure P_1 and the time the solenoid valve remains open. Lower P_1 s, higher P_4 s and higher valve opening times will lead to stronger shock, increasing temperature and pressure. Changing these parameters, different shock conditions can be achieved.

The driver gas pressure (P_4) represents the pressure behind the diaphragm or piston that generates the shock wave. Higher P_4 values result in increased energy transferred to the driven gas, leading to higher temperature shock waves. By adjusting P_4 , the temperature of the shock can be controlled, influencing the resulting temperature and pressure changes in the gas mixture.

Similarly, the driven gas pressure (P_1) affects the behavior of the shock wave. Lower P_1 values allow for a larger pressure difference between the driver and driven gases, promoting a higher temperature shock. This pressure difference contributes to the compression and heating of the driven gas as the shock propagates.

The duration of the solenoid valve opening determines the time interval during which the gases can interact and exchange energy. Longer valve opening times enable a more extended period of gas mixing and energy transfer, resulting in enhanced shock effects. By adjusting the valve opening time, the duration of shock wave propagation and its interaction with the gas sample can be controlled in this way.

Together, these parameters provide a means to manipulate the shock conditions and explore different aspects of gas dynamics, such as compression, expansion, temperature changes, and pressure variations. By systematically varying P_4 , P_1 , and valve opening times, the effects of shock intensity on chemical reactions, fluid flow, and other phenomena of interest are controlled.

The experiments in the shock tube were consistently conducted at a frequency of 0.125 Hz. This frequency refers to the rate at which shocks were generated and data were acquired during the experimental process.

Operating the experiments at a specific frequency provides several advantages. Firstly, it allows for controlled and reproducible conditions, ensuring consistent shock wave generation and data collection across multiple trials. This standardization minimizes variations that may arise from irregularities in the experimental setup or fluctuations in operational parameters.

The chosen frequency of 0.125 Hz strikes a balance between experimental efficiency and data resolution. It provides a sufficiently high frequency to capture an adequate number of shocks within a reasonable time frame, enabling the gathering of a substantial amount of data for analysis. At the same time, the frequency is not excessively high, avoiding potential challenges associated with rapid data acquisition and processing.

3.2 Mixture preparation

The mixture was created by following a specific procedure. C_2H_5I (Sigma-Aldrich, 99% purity) in its liquid form was connected inside a schlenk tube, which was then integrated into a system featuring vacuumed manifolds that were connected to a tank. A degassing process was done, which involved connecting the schlenk tube to a vacuum source. To eliminate dissolved gases and volatile impurities, the degassing process was performed twice for 4 minutes. After degassing, C_2H_5I was carefully introduced into the system until the desired quantity was attained. Subsequently, argon gas was added to the mixture until it reached a 1% composition. To ensure thorough mixing and potential interactions between the components, the mixture was allowed to rest undisturbed for approximately 45 minutes within the tank. This meticulous preparation process ensured the formation of a well-mixed and suitable mixture for the intended purposes.

The same procedure as mentioned earlier was utilized for CF_3I (Sigma-Aldrich, 99% purity). However, since CF_3I is already in a gaseous state at room temperature, it was directly introduced into the system without the need for additional steps such as degassing.

The driver section was filled with Praxair ultra high purity helium.

To ensure the accuracy and composition of the mixture, it underwent analysis using gas chromatography (GC). The prepared CF_3I sample (3%) was introduced into the Agilent MS 5977B detector through a sampling line (See Figure 7), the 6-way pneumatically operated gas sampling valve and PLOT U column. The sampling line setup uses a high accuracy temperature controller and a MKS capacitance manometer, which can read pressures up to 1000 Torr with an accuracy of 0.25% of the measured pressure. The manometer allows for measurements of injection head

pressure of the sample, prior to being injected into the columns, which is used for area normalization of the acquired data. The capacitance manometer also comes into play when sample calibration have to be performed. The components constituting the sampling line setup is developed using Sulfinert® coated components and the sampling line is maintained at a temperature of 140°C to prevent the adsorption and condensation of the samples prior to being injected into the columns. Figure 7 shows the sampling line process flow diagram.

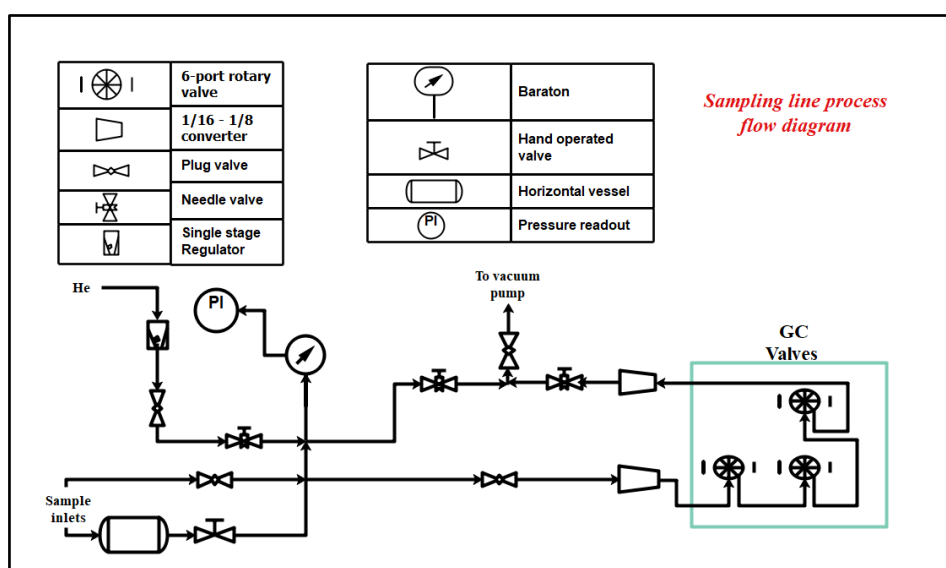


Figure 7: Sampling line process flow diagram.

Trifluoroiodomethane was calibrated using the sample obtained from Sigma Aldrich. The pure sample was diluted with Helium to obtain sample concentrations between 3000-6000 ppm for calibration of CF_3I . The relationship between the normalized area (i.e. measured area under the curve divided by the injection pressure) and the corresponding sample concentration is used to obtain a calibration factor that is used to determine the concentration of a new mixture, with the intercept set to zero. Figure 8 shows the plot and the calibration factor obtained after the CF_3I calibration. The calibration mixture was prepared using the same sampling setup mentioned before to ensure consistency in the measurements collected and to reduce the uncertainty in the measurements.

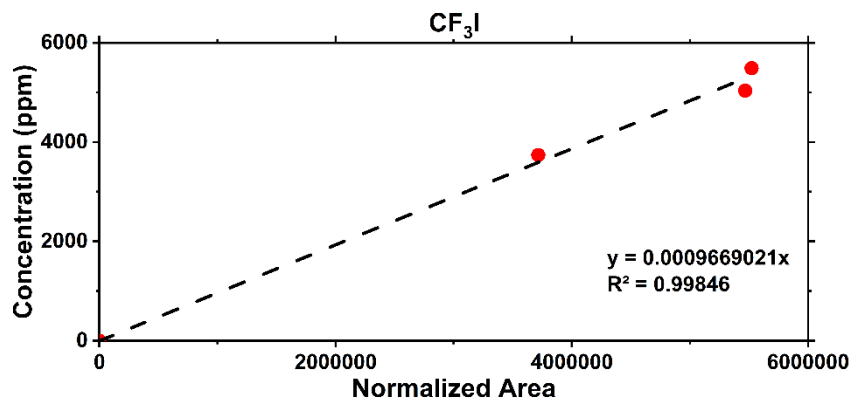


Figure 8: Concentration in ppm from GC.

In this study the sample prepared for the experiments was diluted with Helium to reduce the sample concentration to be ~ 5010 ppm, since the sample prepared was in the range of 30000 ppm (3%) and such high concentration are beyond the detector detection limit and would lead to distorted and saturated detector response. The diluted mixture was allowed to settle for ~ 5 minutes. After performing the run using the GCMS system and performing some calculations such as multiplying the normalized area with the calibration factor, the measured concentration is 5088.97 ppm, which is within the uncertainty of ± 100 ppm, indicating that the mixture prepared for the shock tube experiments have a concentration of ~ 300000 ppm (3%), as shown in Figure 8.

3.3 Laser absorption setup

To carry out the experiments, two experimental methods were employed: fixed wavelength single pass experiments and fixed wavelength double pass experiments. For each of these methods, there is a corresponding setup for the laser diagnostic technique.

The setup for fixed wavelength single pass experiments utilized a fiber-coupled tunable laser diode (Qphotonics QDFBLD-1300-10), which operated at 44°C , at a current of 57.9 mA with the use of a laser diode controller (Arroyo instruments, 6305 ComboSource) to hit a central wavelength of

1315.24 nm. This wavelength was chosen to align with the hyperfine splitting of $2P_{3/2}$ to $2P_{1/2}$ absorption wavelength of iodine, the target species of interest. After being emitted from the source, the laser beam was directed towards a 50:50 cage cube-mounted beam splitter (CCM5-BS018, Thorlabs). The beam splitter divided the laser beam into two distinct paths: one path allowed half of the laser beam's intensity to pass through the shock tube, enabling it to interact with the gas sample inside; the other path directed the remaining half of the laser beam's intensity towards the first detector (PDA10CS2, Thorlabs), known as the reference detector. The reference detector measured the initial intensity (I_0) of the laser beam before it interacted with the gas sample. This measurement served as a reference baseline for subsequent intensity comparisons. The voltage signal was measured on National Instruments 6376 data acquisition system. After passing through the shock tube, where the absorption of the laser light by iodine molecules present in the gas sample happened, the laser beam proceeded towards a parabolic mirror positioned at the other side of the endwall. The parabolic mirror (MPD149-M01, Thorlabs) focused the laser beam, which was then directed towards another detector. The detector positioned to receive the focused beam measured the transmitted intensity of the laser (I_1). By quantifying the intensity of the laser beam after its interaction with the gas sample, this detector provided information regarding the amount of laser light absorbed by iodine molecules, using Beer's law (Equation 1). A schematic of the single pass setup is shown in Figure 9 below.

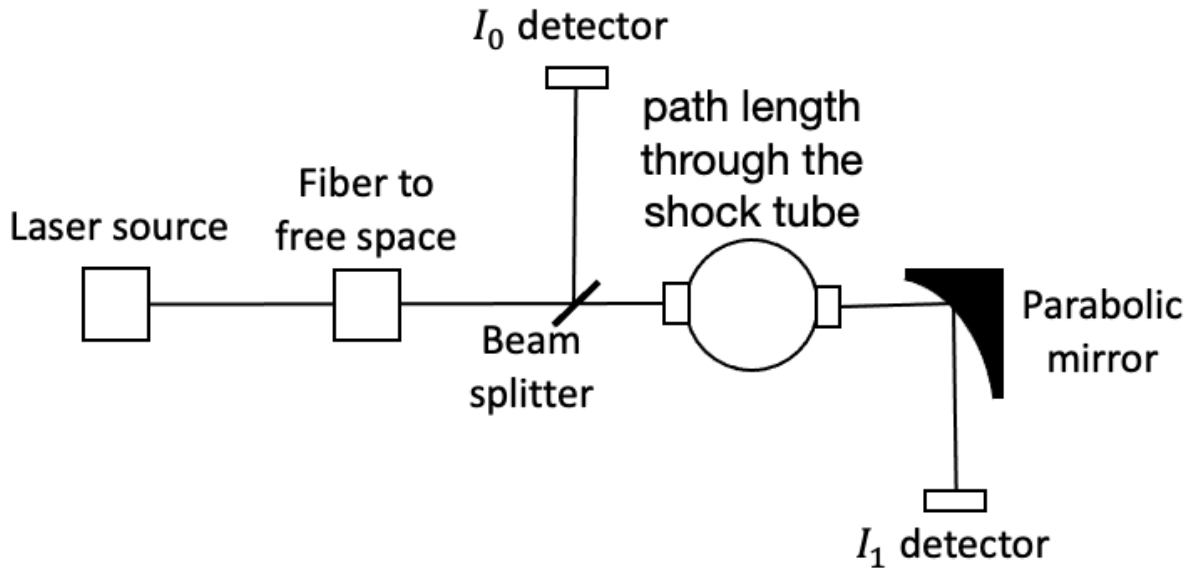


Figure 9: Schematics of the laser absorption diagnostic setup for fixed wavelength single pass experiments.

In the fixed wavelength double pass setup, the experimental configuration was similar to that of the fixed wavelength single pass's one, with some key differences. A beam reducer (BE06R - 6X, Thorlabs) was placed in front of the laser source to reduce the beam diameter and optimize alignment precision. The laser beam was again split into two equal parts by a beam splitter (CCM5-BS018, Thorlabs), with one half passing through the shock tube and the other half directed towards the reference detector (PDA10CS2, Thorlabs) to measure the initial intensity (I_0). However, in this setup, a retroreflector was introduced after the laser beam passed through the shock tube. The retroreflector allowed the laser beam to retrace its path: it underwent a second time through the gas sample within the shock tube, increasing the path length. The returning beam from the retroreflector then passed through the same beam splitter once more and was directed towards another detector, referred to as the transmitted intensity detector, which quantified the transmitted intensity (I_1). For these experiments, the window section of the shock tube was changed, and a

new pair of wider windows was used, in order to facilitate the alignment. The pressure transducer connected to the new endwall is PCB CA102B06, which is not thermally insulated.

A schematic of the setup is shown in Figure 10.

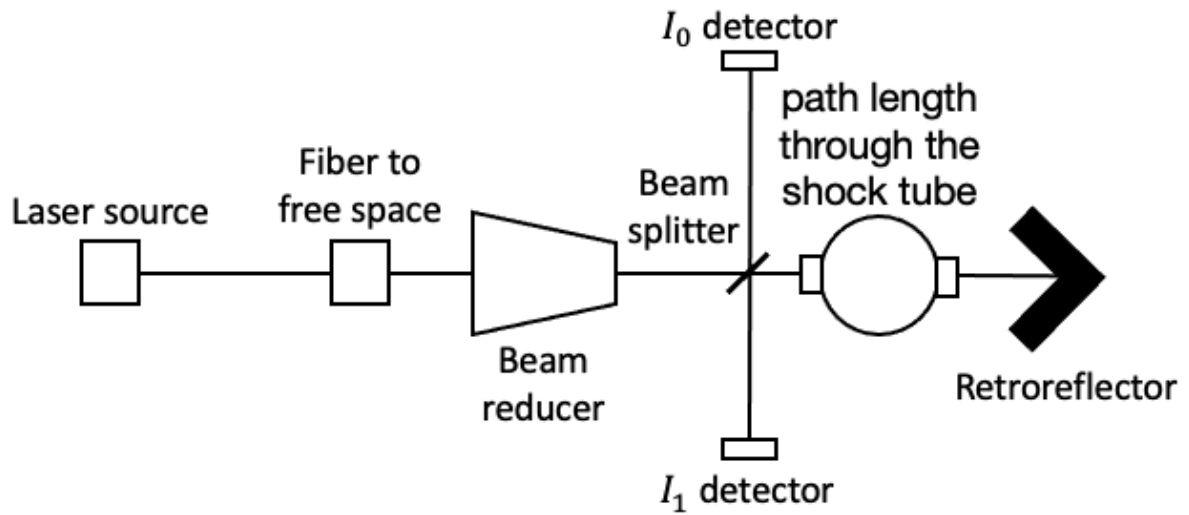


Figure 10: Schematics of the laser absorption diagnostic setup for fixed wavelength double pass experiments.

The final setup is shown in Figure 11.

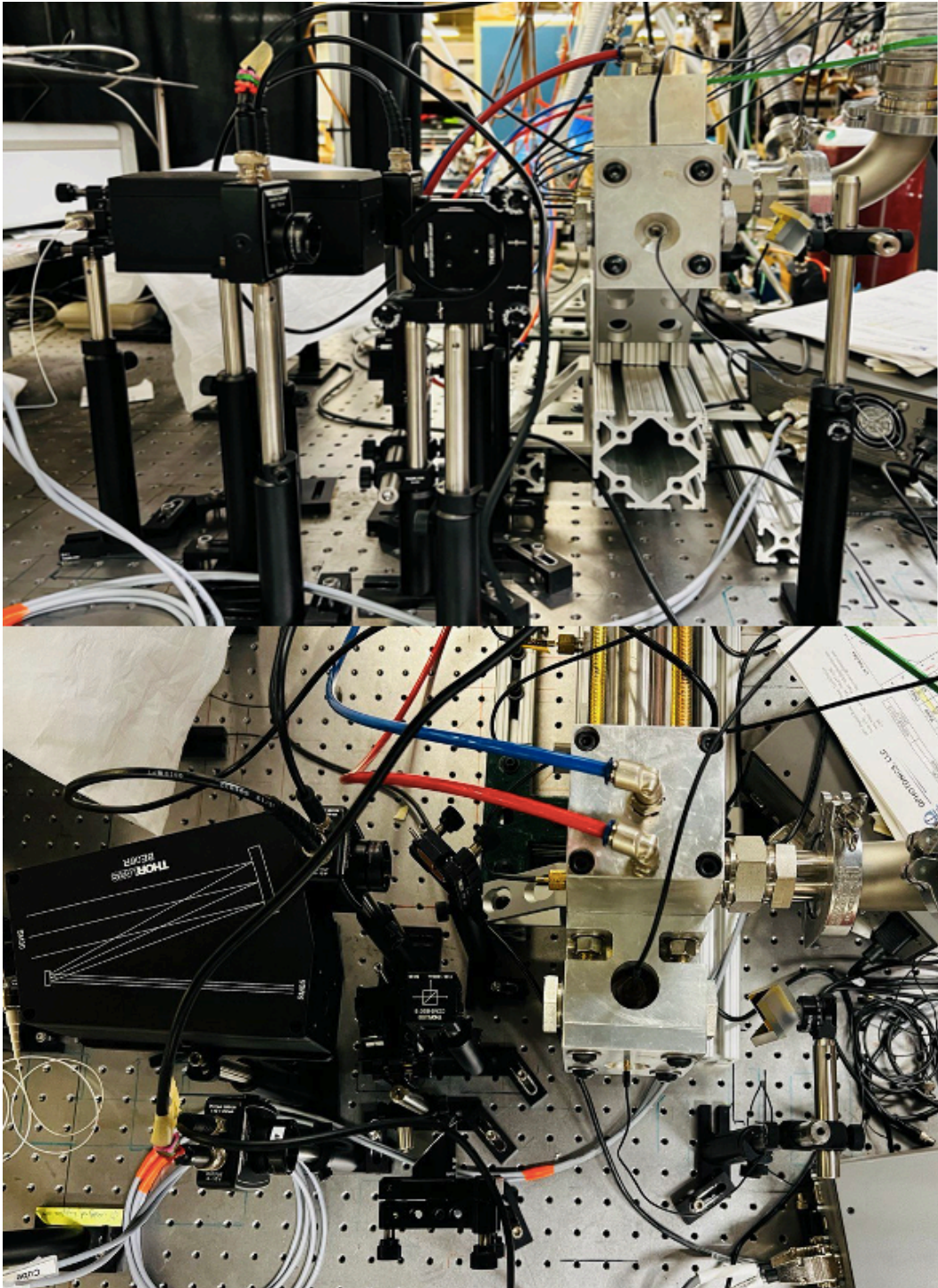


Figure 11: Final setup double pass experiments.

3.4 Diagnostic technique: laser absorption spectroscopy

Laser absorption spectroscopy is based on the interaction between a laser beam and specific gas molecules present in a sample. When the laser beam passes through the sample, the molecules selectively absorb light at specific wavelengths corresponding to their unique energy levels. The relationship between the transmission of light by a sample and the concentration of the absorbing species is governed by the Beer-Lambert law, in Equation 16.

$$\frac{I_1}{I_0} = \exp(-\sigma_\lambda NL) = \exp(\alpha), \quad (16)$$

where I_1 is the transmitted intensity of the laser, I_0 is the reference intensity, σ_λ is the absorption cross-section at wavelength λ in (cm^2/mol), N is the species' concentration (mol/cm^3) and L is the path length (cm). The product $\sigma_\lambda NL$ is equivalent to absorbance α , which is dimensionless..

To accurately measure atomic iodine, an investigation of iodine's absorption cross-section and its spectrum was performed. This allowed to determine the specific wavelengths at which iodine absorbs light, enabling the measurement of iodine concentration. In their study, Murzyn et al. [24] scanned a tunable diode laser to target the hyperfine splitting of $2P_{3/2}$ to $2P_{1/2}$ at wavenumbers 7603.1384 cm^{-1} , 7603.2794 cm^{-1} , 7603.3450 cm^{-1} .

These results were then used to simulate the iodine spectrum and calculate the absorbance.

From Beer-Lambert law (Eq 16), the absorbance α can be defined as Equation 17:

$$\alpha = -k_\nu \cdot L \quad (17)$$

Where L is the pathlength, and k_ν is defined as in Equation 18:

$$k_\nu = S_{12} \cdot \phi(\nu) \quad (18)$$

Where S_{12} is the linestrength, and it represents the intensity of a specific absorption transition from 1 to 2, and $\phi(\nu)$ is the lineshape. Lineshape refers to the distribution of intensity of emitted or absorbed light as a function of wavelength.

The lineshape is assumed to be a Voight profile., which is s a convolution of a Gaussian profile and a Lorentzian profile.

The calculation of linestrength, from [25], is shown in Equation 19:

$$S_{12} = \frac{\lambda^2}{8\pi} n_1 A_{21} \frac{g_2}{g_1} \left[1 - \exp\left(-\frac{h\nu}{kT}\right) \right] \quad (19)$$

where, λ is the linecenter wavelength , n_1 is the number density of absorbing species, A_{21} is the Einstein coefficient for spontaneous emission, which characterizes the transition probability between the energy levels of the spectral line, g_1 is the lower state of degeneracy, g_2 is the higher state of degeneracy, $\frac{g_2}{g_1}$ is the ratio of the degeneracy of states, which accounts for the degeneracy of the states involved in the transition, h is Planck's, ν is the wavenumber of the transition, constant, k is the Boltzmann constant, T is the temperature.

The number density of iodine is obtained by putting (19) into (18), into (17), into (16).

With these equations, the calculation of the absorption cross section is possible.

The values used are taken from Murzyn et al. [24], and are listed in Table 1, below:

Table 4: Values for the evaluation of the iodine spectrum from [24].

Parameter	Value	Unit
λ	1315.25	nm
E_{lower}	0.11300	cm^{-1}
g_1	7	-
g_2	9	-
Q	24	-
A_{21}	3.66883	s^{-1}

The resulting profile of the simulated iodine absorbance spectrum is shown in Figure 12.

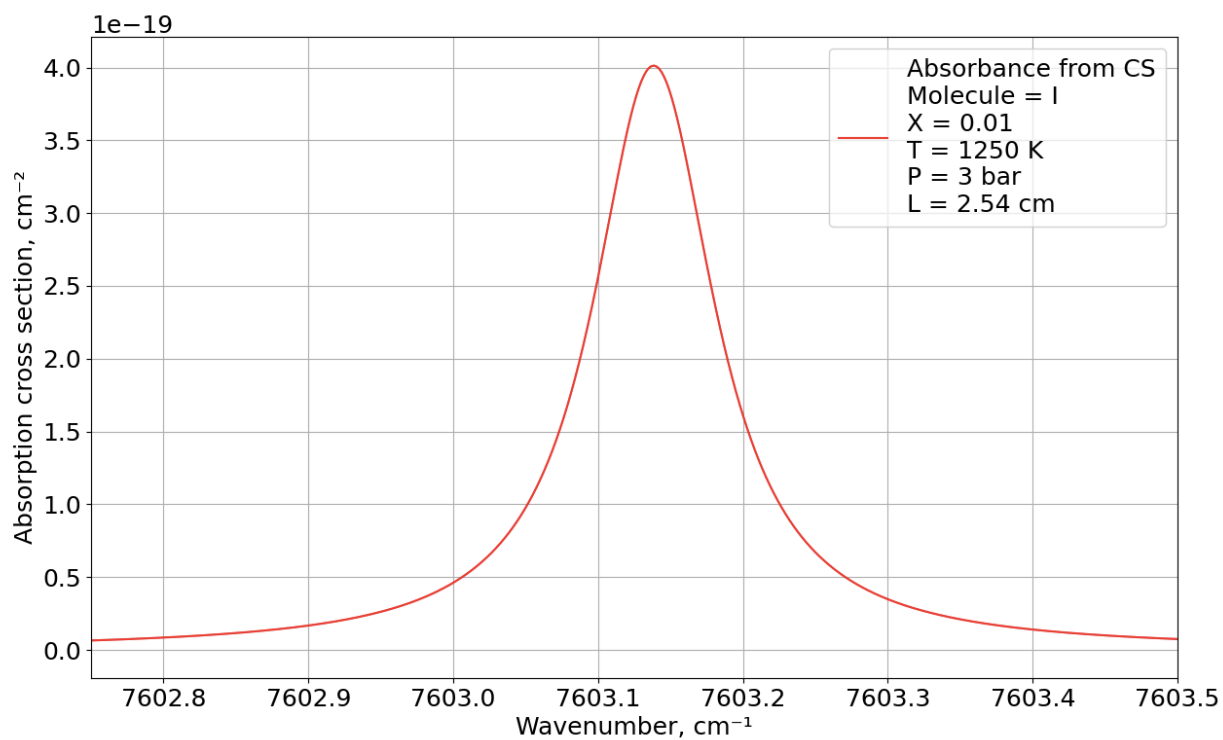


Figure 12: Absorption cross section of iodine at a central wavenumber of 7603.1384 cm^{-1} .

The modeling of the absorption cross section is fundamental in the modelling process for the understanding of the behavior of the simulated system. By incorporating the calculated absorption cross section into simulation models, accurate predictions of the expected absorbance behavior can be made under various conditions. This facilitates the comparison between simulated and experimental absorbance, enabling comprehensive validation and interpretation of the findings.

3.5 Beam steering and handling low absorbances

One of the main challenges in experimental measurements is the uncertainty of whether a reduced transmission is solely due to absorbance or other factors. To address this challenge, various methods can be employed to ensure that the observed reduction in transmission is indeed attributed to absorbance. These methods include enhancing the signal strength relative to noise. Distinguishing between absorption at a resonant frequency and non-resonant effects, such as beam steering, is crucial. Figure 13 shows the raw signal from an individual double pass experiment.

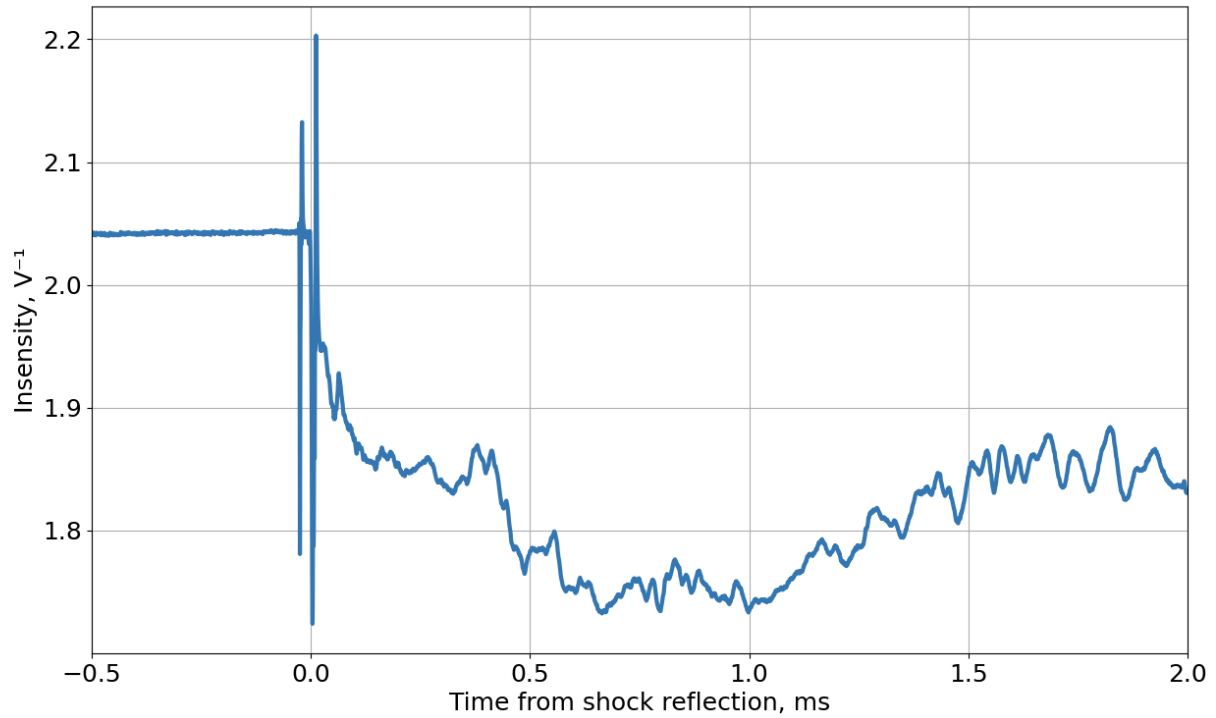


Figure 13: Signal of an individual double pass experiment.

To gain a better understanding of beam steering effects and quantify the uncertainties associated with absorbance measurements, experiments at non-resonant wavelengths were conducted. By performing measurements at wavelengths where iodine does not exhibit strong absorbance, the contribution of beam steering can be isolated and analyzed.

The non-resonant wavelength experiments serve as a reference for assessing the uncertainties related to beam steering. By comparing the transmission behavior at non-resonant wavelengths with the expected behavior based on beam steering effects, the degree of deviation can be quantified and error bars for absorbance measurements can be established. The average of 100 non-resonant experiments is shown in Figure 14.



Figure 14: Average intensity detected on 100 non-resonant experiments.

Figure 14 shows the data points of the average of 100 non-resonant experiments. This is used to estimate the error bars in the analysis. Since there is no interaction between iodine and the laser at this wavelength, the intensity detected should ideally be constant. This is not the case due to phenomena like beam steering. As it can be seen, at higher times corresponds higher deviation.

4. Modelling

4.1 Processing technique

The analysis of experimental data assumes a pivotal role in extracting the rate constant for the study. This section introduces the processing techniques employed to analyze the data collected from experiments, with the primary goal of extracting the rate constant for the thermal dissociation of CF_3I . These processing techniques were used both for C_2H_5I and CF_3I systems.

Figure 15 shows an individual experiment ran using a 2% CF_3I mixture.

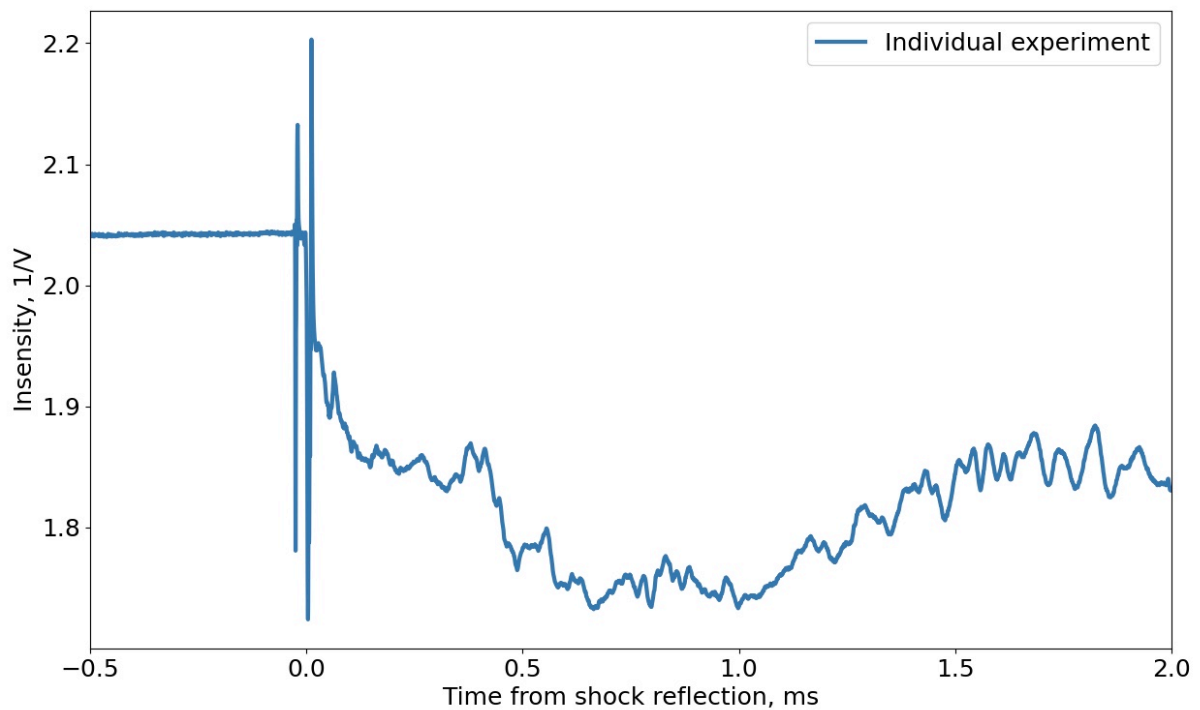


Figure 15: Signal intensity for an individual experiment.

Figure 15 illustrates that, when a shock wave arrives, the signal shows some spikes manifest as sudden. These are called Schlieren spikes and they are attributed to the rapid changes in density and refractive index induced by the shock wave's passage. After the shock wave arrives, the

observed signal in Figure 15 exhibits a decrease in intensity. This decrease can be attributed to the phenomenon of light absorption by iodine molecules present in the gas.

The Time-of-Arrival sensors detect pressure changes, determining the moment when the shock wave reaches them. The recorded TOA data serve for calculating the velocity of the shock wave. With the known distances between the TOA sensors, the time difference between the shock wave's arrival at two sensors can be measured. This time difference enables the calculation of the shock wave's velocity.

In the initial stage of data processing, the first step was the exclusion of inadequate experiments from the dataset. By examining the collected data, experiments that exhibited anomalies in time of arrivals were identified as insufficient and were therefore discarded.

The second step consisted in dividing the experiments in the dataset and averaging them: this process is called binning.

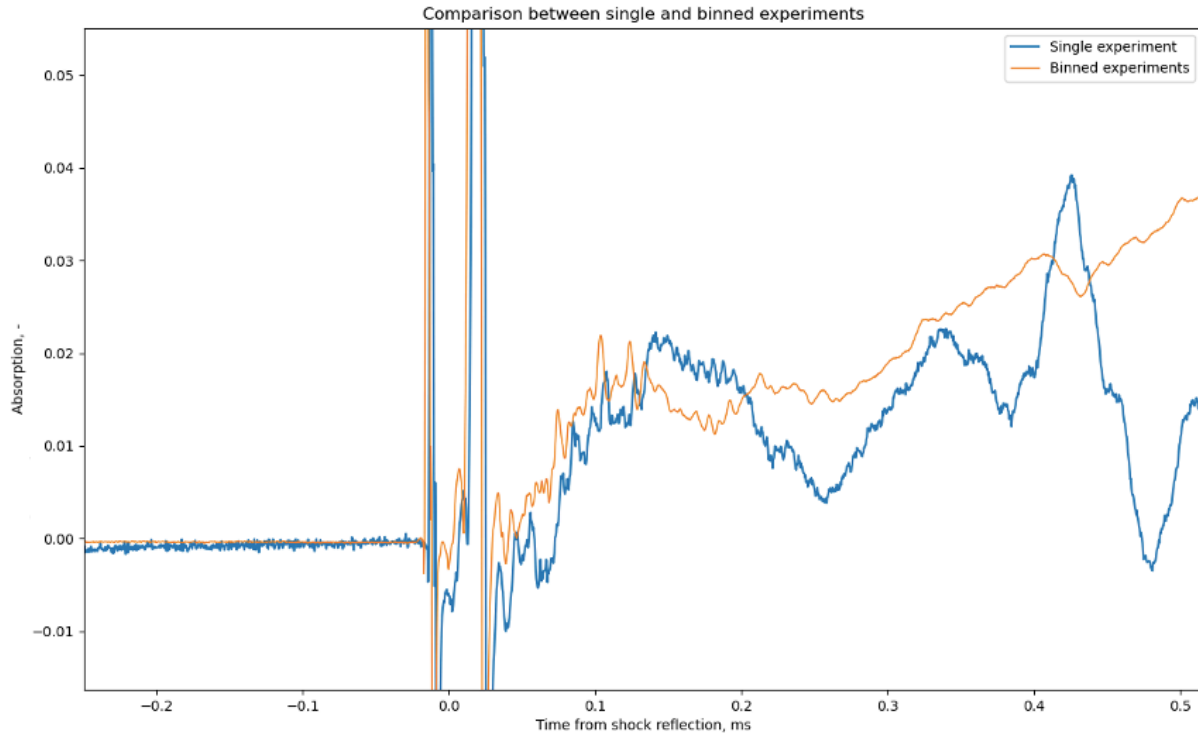


Figure 16: Comparison between the absorption signal of a single experiment and a group of binned experiments.

As shown in Figure 16, binning proves to be advantageous for this study as it can address the inherent random deviations encountered from experiment to experiment. By employing binning techniques, these random variations are averaged out, resulting in a more robust and reliable signal. The process of binning allows for a smoothed representation of the data. This smoothing effect minimizes the impact of random deviations and significantly improves the signal-to-noise ratio. Furthermore, signal averaging over multiple experiments can significantly improve the reliability of the measurements. Averaging subsets of experiments is beneficial for the analysis because it also mitigates random variations or errors present in individual experiments, leading to a more reliable representation of the signal. One of the sources of deviation of the signal is beam steering, which consists in a change in refractive index inside of the shock tube because of the

thermal gradients and species changes inside of it. This results in a greater uncertainty in the signal.

Because of the beam steering, offline experiments were run as well: these experiments are conducted at a wavelength where iodine presents no absorption feature, in order to quantify the entity of the beam steering. These experiments were then used to add error bars to the experimental curves.

In the process of binning the experiments, the criterion used to group experiments was based on the temperature within the region behind the reflected shock wave, which is referred to as region 5. Experiments were categorized into sets based on the temperature values measured in that region (T_5) since shocks with similar T_5 s also show similar trends in pressure profile and velocities.

Figure 17 shows the shock velocities for two different binned groups: group 1 is the group at lowest temperature and group 10 is the group at highest temperature.

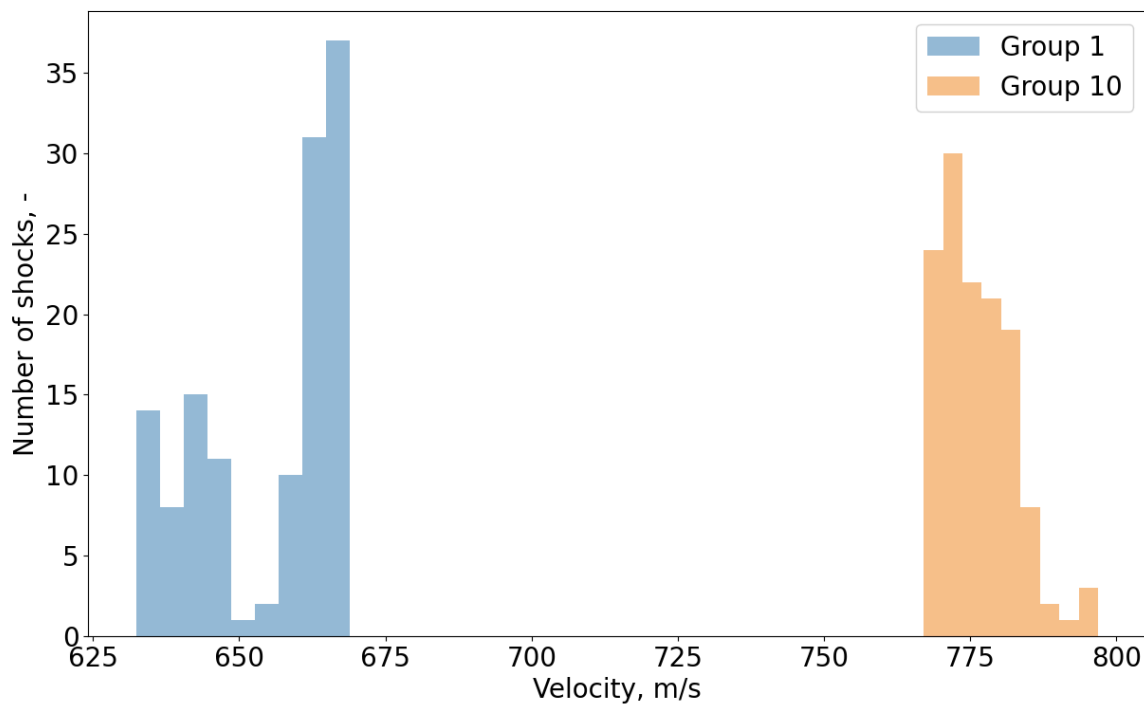


Figure 17: Shock velocities within two different groups: group 1 (low temperature) and group 10 (high temperature).

As it can be seen, the shocks within each group have similar velocities. Figure 18 shows the pressure profiles for two different binned groups: group 1 is the group at lowest temperature and group 10 is the group at highest temperature.

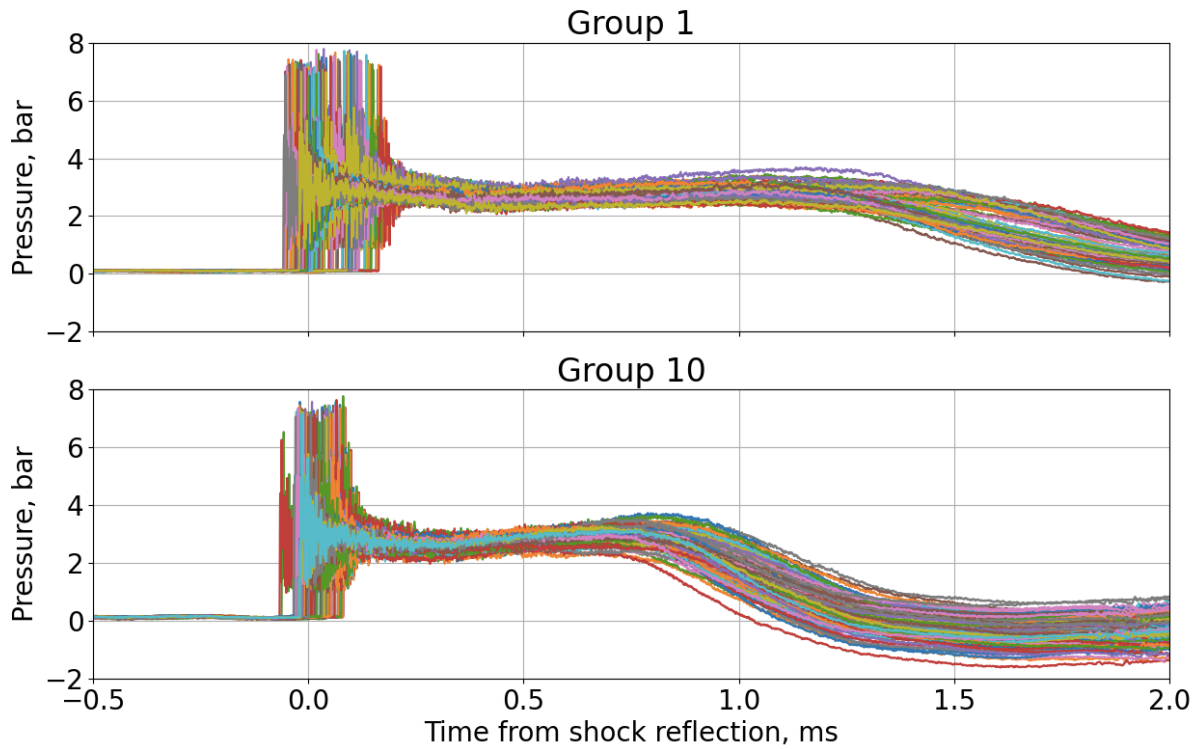


Figure 18: Pressure profiles within two different groups: group 1 (low temperature) and group 10 (high temperature).

As it can be seen in Figure 18, the shocks within each group also have similar P5 trends.

The code used for creating binned groups distributed the shocks evenly across them by saving T_5 value for each shock and assigning boundaries that ensure an almost equal number of shocks in each group. By using these calculated boundaries as thresholds, each shock was assigned to the appropriate group based on its temperature. The resulting grouping scheme ensured a balanced distribution of shocks. For CF_3I , out of 1296 experiments, 10 groups were created, each with about 130 shocks, as shown in Figure 19.

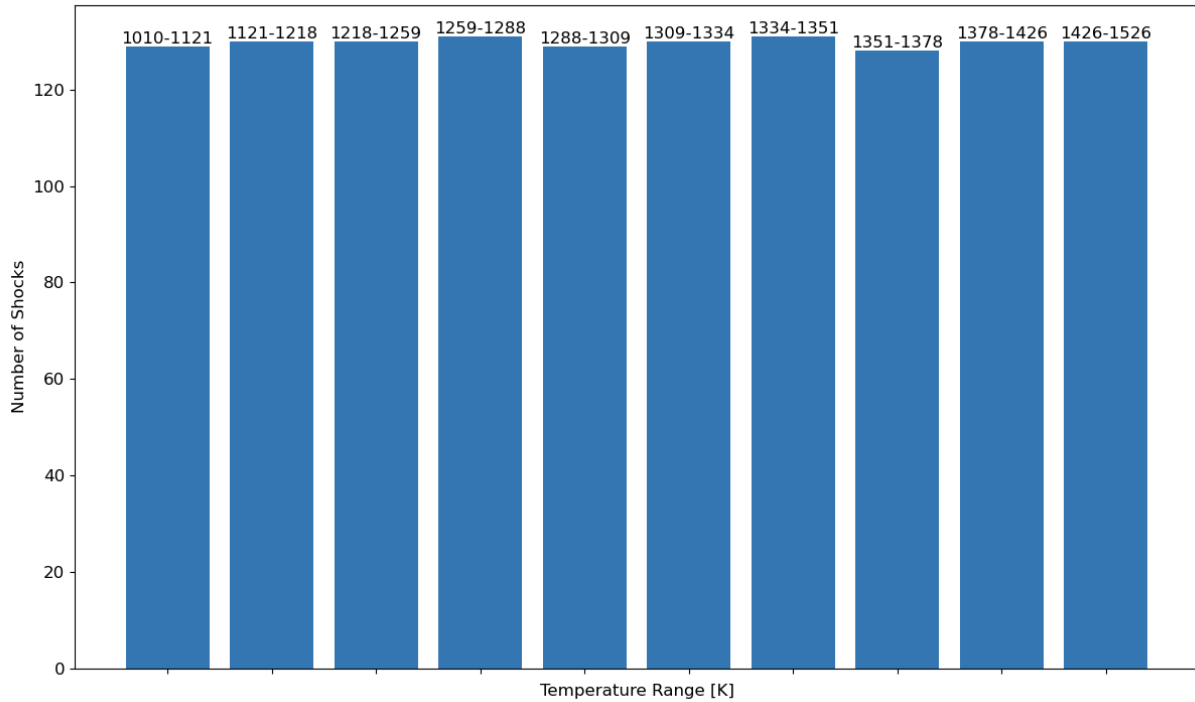


Figure 19: Shocks distribution for each group and its temperature range in CF_3I experiments.

After dividing the shocks into groups, the code aligned and averaged within each group the pressure signals P_5 , the reference intensity of the laser I_0 , and the intensity of the laser after passing through the shock tube I_1 . Aligning the experiments is necessary because slight variations in the shock formation time can occur for each experimental run. In order to compare and average the results across multiple experiments, it is important to align them based on a common reference point. The alignment process involves identifying the time of shock arrival in the experimental data that serves as a reference. By aligning the experiments based on this point, the time axis can be synchronized and ensure that corresponding data points are compared accurately.

For each group, the code identified a reference time for every experiment within that group, which served as a common time point for alignment. It did this by finding the index of the first time point that corresponded to the reference shock within each data set. This ensured that the shocks were

synchronized in time. Next, the code created arrays to store the aligned and averaged pressure signals. It initialized these arrays with zeros and kept track of the number of times data were added to each array point using a counting array. This information was crucial for proper normalization later on. For each group, the code calculated the necessary time and index offsets based on the reference shock time. It then replaced the zeros in the aligned pressure array with the corresponding pressure values from the data, taking into account the time and index offsets. This process was repeated for all data sets within the group. To obtain the averaged pressure signal, the code summed up the aligned pressure arrays from each data set. Additionally, it summed up the counting arrays to determine the number of times data were added to each array point. Finally, the code normalized the averaged pressure array by dividing each element by the corresponding count value. This step ensured that the averaging process did not introduce any bias towards certain time points or data sets.

Switching from single pass to double pass experiments, the window section, and consequently the pressure transducer at the endwall, were changed. Figure 20 illustrates the pressure data obtained from these two different pressure transducers: pressure transducer PCB CA102B06 (blue curve, used in single pass setup) and pressure transducer PCB 105C12 (orange curve, used in double pass setup). The blue curve represents the pressure readings from transducer PCB CA102B06, which has a lower precision compared to transducer PCB 105C12, since the first one is not thermally insulated while the second one is. In order to compensate for the lower precision of transducer PCB CA102B06, an alternative pressure curve was obtained from a single pass experiment. The pressure curve from the single pass experiment was chosen based on its similarity in terms of the temperature (T_5) and velocity to the average values of T_5 and velocity obtained from the binned

experiments. To ensure consistency, the chosen curve was then scaled to match the initial pressure value of the reference pressure curve.

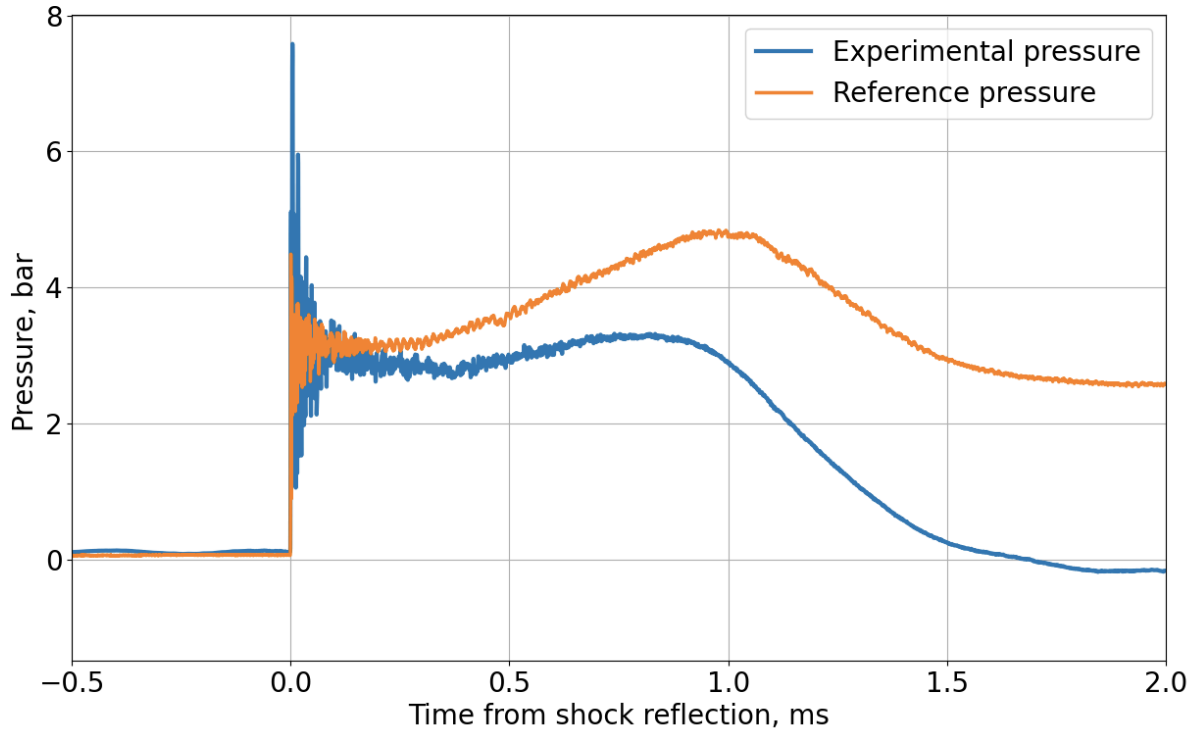


Figure 20: Pressure profiles from a single pass experiment (orange curve) and from the average of one set of double pass experiments (blue curve).

Comparing the two curves, it is evident that the reference pressure curve exhibits higher pressure values throughout the measured range. This discrepancy in pressure values between the two curves highlights the limitations in precision between the pressure transducer used in the experiments, which is the reason why pressure curves from single pass experiments were used.

After aligning averaged I_0 , and I_1 profiles, and matching the new pressure profile, two peculiar time instants were identified. These points are shown in Figure 21.

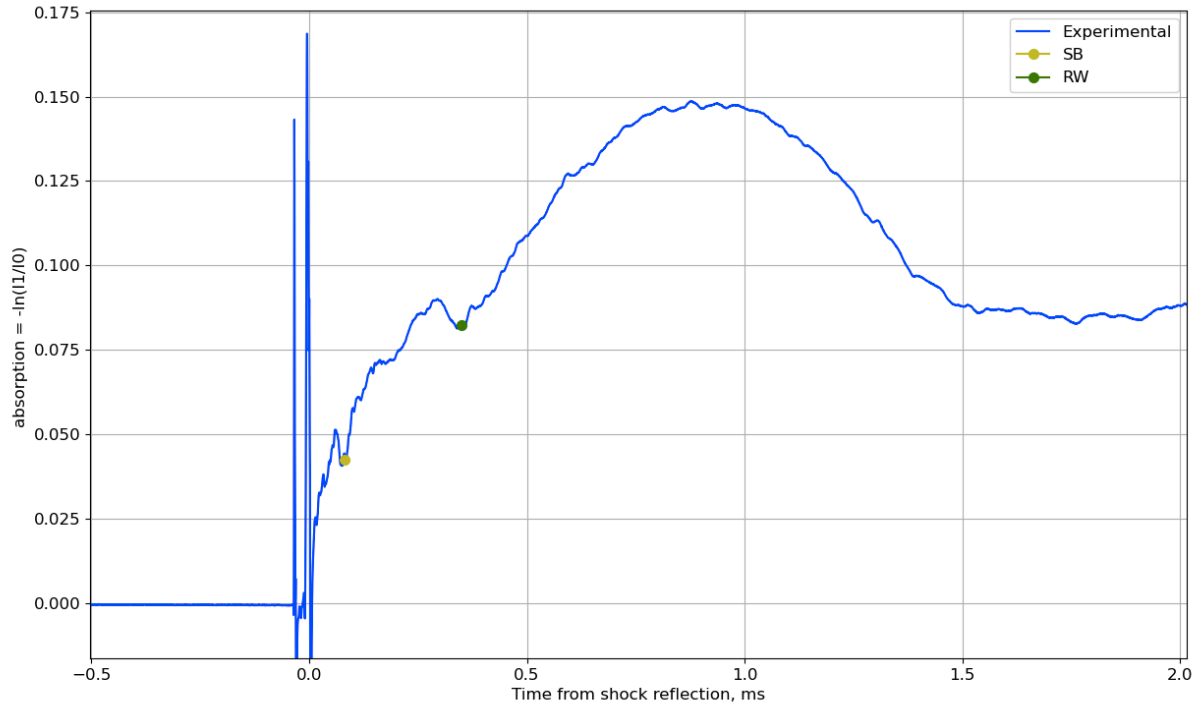


Figure 21: Absorption curve for one set of CF_3I experiments. The yellow dot SB stands for stagnation bubble point and RW stands for reflected waves point, after which this phenomenon becomes more relevant.

The first point, the yellow dot in Figure 21, could be stagnation bubble is formed. Behind the incident shock, there is a density variation, which is mainly caused by the formation and growth of the boundary layer. This boundary layer develops as the high-speed flow interacts with the surface. However, in the region behind the reflected shock, the density variation becomes more intricate due to the interaction between the reflected shock and the expanding boundary layers. This interaction can give rise to several phenomena, including the bifurcation of the shock [26]. If the boundary layer lacks sufficient momentum to pass through the normal shock, bifurcation can take place. This results in a splitting or branching of the flow pattern. The idealized model suggests that the energy-deficient boundary layer gas accumulates behind the first oblique shock, and then a second oblique shock returns the flow parallel to the wall. The presence of a vortex sheet separates the moving fluid from the stagnant fluid at the endwall. Additionally, this can lead to the

formation of stagnation bubbles, which are localized regions of flow separation immediately behind the reflected shock. A stagnation bubble is a region of trapped and compressed gas that forms at the closed end of the driven section of the tube during the shock wave propagation. These variations introduce additional uncertainties into the data, making it challenging to obtain an accurate fit. The recovery of the signal quickly after this first valley does not significantly impact the assignment of the absorption before and after it. This rapid recovery suggests that the perturbation caused by this event is short-lived, and the system returns to its original state quickly. Therefore, the absorption observed around this point can still be confidently determined.

However, the presence of the second valley introduces a complication in the understanding of the absorption at that specific point. The occurrence of this second valley indicates the presence of a contact surface or a reflected rarefaction wave, which can significantly influence the behavior of the system. The exact position of this second valley, the green dot in Figure 21, can disrupt the interpretation of the absorption at that particular location. This point that is observed that in the last region of the experimental data, at times higher than 0.5 ms, suggests that additional phenomena such as a contact surface or a reflected rarefaction begin to influence the measurements. Due to the presence of these complex wave interactions, conducting an accurate analysis in this region becomes challenging. Consequently, the focus of the analysis is initially limited to the first two regions.

4.2 Prediction method

The fitting procedure aims to minimize the error between the simulated and experimental data by adjusting the rate constant value. This adjustment process involves allowing the rate constant to vary within two boundary values. The fitting is performed for 10 points, each representing a

group of binned experiments. By iteratively refining the rate constant value, the fitting procedure aims to optimize the agreement between the simulated results and the experimental measurements for each of the 10 groups. The procedure is the following:

1. Variation of k for each experiment

This loop involves varying a scaling factor for the rate constant (k_1) in each set of binned experiments to optimize its value.

- 1.1 Initialization:

A custom pressure dependent reactor is initialized using initial temperature derived from chemical thermometry, pressure history, initial composition, and a chemical mechanism specific to CF_3I . The simulation predicts the behavior of CF_3I based on reactor concentrations and the pressure/temperature dependent parameters. The rate constant is initially guessed using the mechanism file value.

- 1.2. Comparison:

The experimental and simulated data are compared over the specified test time. The least squares error between the simulated and experimental data is minimized by iteratively adjusting the scaling factor of k_1 until the error falls below a specified tolerance. The value of k_1 is recorded for each experiment.

Shaik et al. [27] utilize the same process in their research, with the difference that their fitting procedure involves an outer loop that checks the temperature dependence within each experiment and ensures it matches that of the sets of experiments. However, in this particular case, the

refinement process is not necessary. The reason for skipping the refinement step is the consistency in the temperature range across the binned experiments.

With the results obtained from the fitting process, an Arrhenius plot can be generated to further analyze the thermal dissociation kinetics of CF_3I . The Arrhenius plot is a graphical representation of the rate constant as a function of temperature. By varying the temperature and performing the experimental measurements, the rate constant values can be obtained for different temperature points. These experimental rate constant values can be plotted against the corresponding temperatures, creating an Arrhenius plot. By comparing the experimental rate constant with the literature rate constant and analyzing the best-fit line on the Arrhenius plot, it is possible to assess the agreement between the experimental results and the previously reported data.

A schematics of the analysis technique is shown in Figure 22.

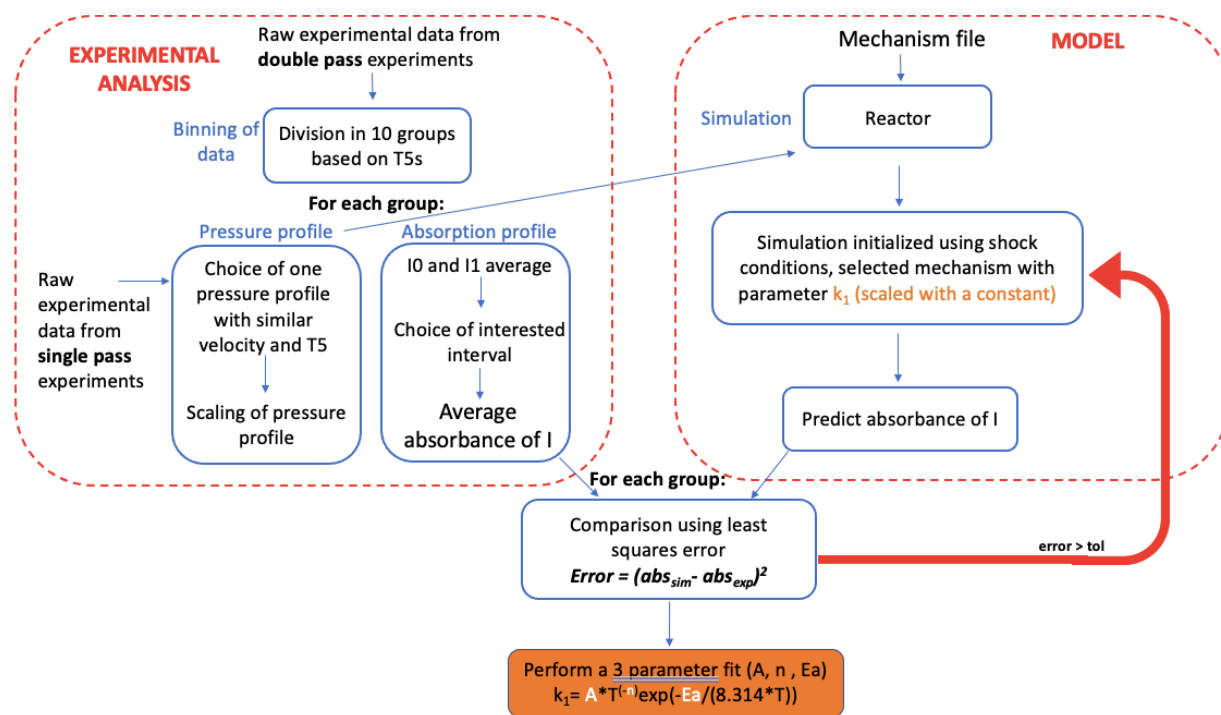


Figure 22: Schematics of the analysis technique.

5. Experiments and results

5.1 Experiments conducted

The consistent frequency ensures that the experimental results are comparable and facilitates the identification of trends and patterns in the data.

Table 5 sums up the experiments run.

Table 5: Experiments run

System	Number of experiments	Composition (%)	Temperatures (K)	Pressure (bar)
CF_3I	1296	2	1010 – 1526	3
	400	3	1057 - 1496	3
C_2H_5I	900	1	1173 - 1495	3
	300	0.5	1122 - 1534	3

For CF_3I , initial experiments were conducted using a composition of 3%. However, during the experimental process, it was observed that also 2% composition provided favorable results. Therefore, 2% mixture was used, in order to run more experiments. For C_2H_5I , initial experiments were carried out using a concentration of 0.5%. However, it was found that the resulting signal intensity was too low to obtain reliable data. As a result, a decision was made to increase the composition to 1% in order to enhance the signal strength and improve the accuracy of the measurements. Consequently, the analysis and interpretation of the experimental results were solely based on the data obtained from the 1% concentration level, while disregarding the 0.5% concentration.

5.2 Evaluation of the three laser configurations

In the pursuit of a comprehensive understanding of the dynamics of the system, three experimental methods were employed: fixed wavelength single pass experiments and fixed wavelength double pass experiments. These methods allowed for the exploration of different aspects of the system and the precise measurement of key parameters.

Single pass experiments formed the foundation of the experimental approach. While single pass experiments served as a fundamental approach in studying shock wave dynamics, they had a notable drawback: the signal intensity obtained from these experiments was often too low for accurate and reliable measurements. This limitation stemmed from the fact that the laser beam only interacted with the gas sample in the shock tube during a single pass, resulting in a relatively weak absorption signal. The low signal intensity in single pass experiments posed challenges in accurately quantifying as the concentration of iodine and, consequently, into determining the rate constant of thermal dissociation of CF_3I : the weak signal made it in fact difficult to distinguish the absorption signal from background noise and other sources of interference.

In the fixed wavelength double pass setup, the signal was higher compared to other configuration due to the doubled path length. By employing a double pass configuration, the optical path that the signal traveled through was effectively extended, resulting in increased interaction with the sample. This extended path length allowed for a greater absorption by the sample, leading to a stronger signal. As a result, the accuracy of the experimental data was improved.

Figure 23 shows the absorbance for two individual experiments, one with single pass setup and the other with double pass one.

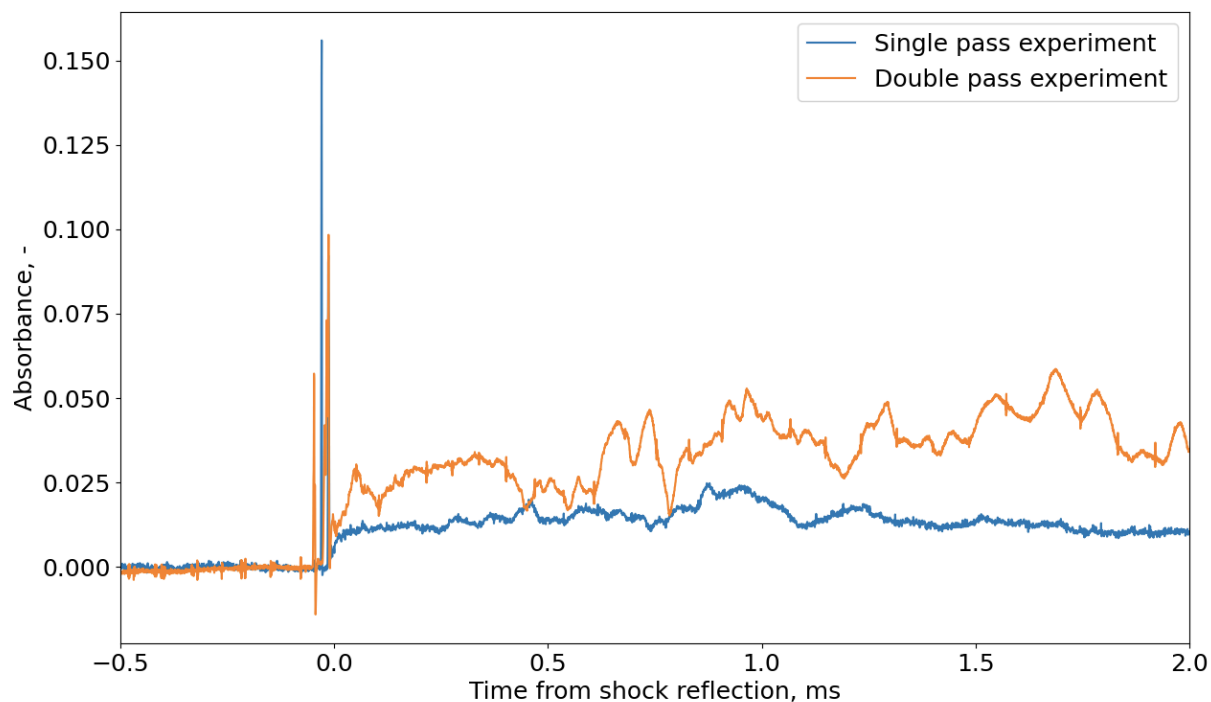


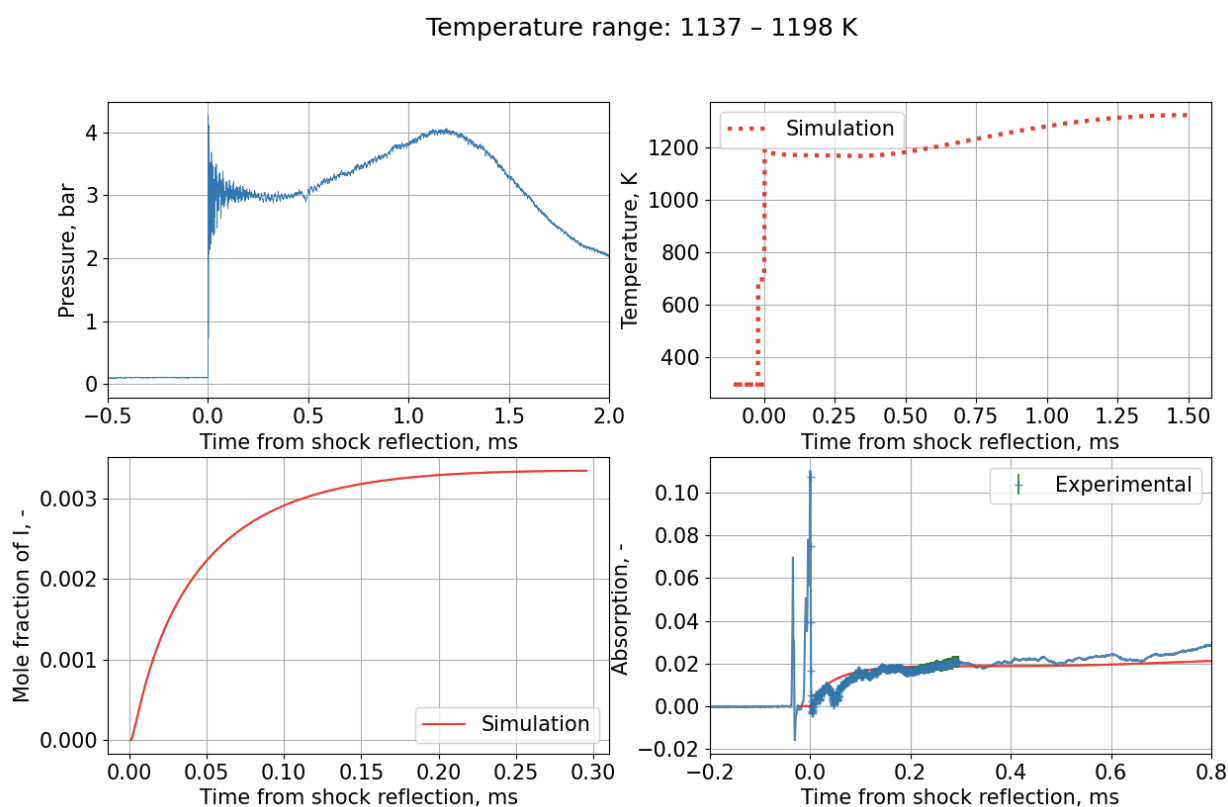
Figure 23: Comparison between a single pass and a double pass experiment at 1% C_2H_5I , $T=1$, 1293 K

Figure 23 underlines the difference in absorbance, and therefore in signal, between the two setups. The double pass technique offers several advantages over single pass measurements, making it a preferred choice in certain experimental setups. By passing the laser beam through the sample twice, the double pass technique increases the optical path length, resulting in higher absorption and improved sensitivity. This increased sensitivity allows for the detection of smaller changes in absorbance and enables more precise quantification of the analyte concentration. Additionally, the double pass setup helps to reduce noise and improve the signal-to-noise ratio of the measurement, leading to more accurate and reliable data. For this reason, double pass was used to carry out the experiments.

5.3 C_2H_5I experiments

The experiments started with the analysis of C_2H_5I system, which is used as a benchmark because of its established rate constants. A total of 900 experiments was run.

Figure 24 illustrates the curve fitting analysis conducted for two different shock groups, each representing distinct temperature ranges. Each plot shows the simulation curve and the experimental curve, with its error bars derived from the offline experiments. The first shock group corresponds to the lowest T5 values (1137 – 1198 K), while the second group corresponds to the highest T5 values (1401 – 1495 K).



Temperature range: 1401 - 1495 K

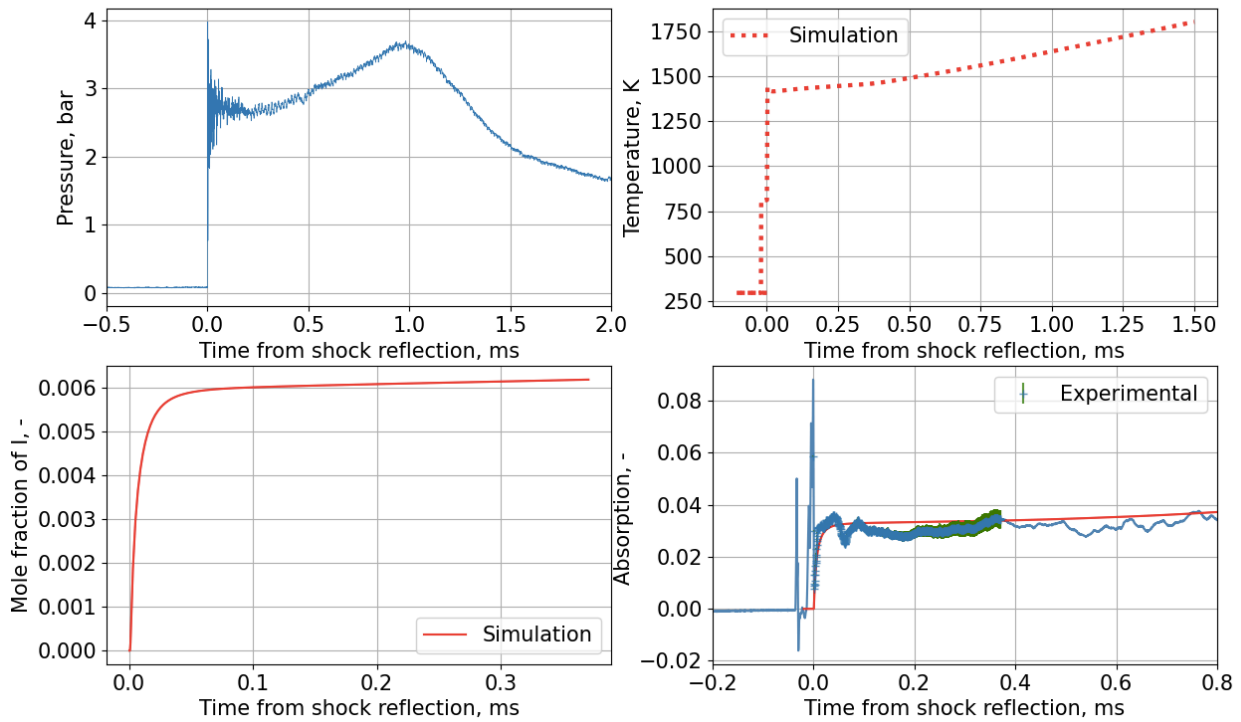


Figure 24: Comparison of simulation and experimental curves for two distinct shock groups representing different temperature ranges, with error bars indicating experimental uncertainties.

In Figure 24, the four subplots represent different aspects of the experimental data and the fitting process. The top left plot shows the adjusted pressure profile, which was scaled to match the P5 value read from the pressure transducer. The top right plot displays the temperature profile, illustrating the variation in temperature over time. The bottom left plot shows the Cantera simulation for iodine mole fraction, which represents the concentration of iodine species present in the system. The bottom right plot illustrates the absorption data obtained from the experiments, which is compared with the Cantera simulation. The fitting process in this case is carried out from zero to the second valley of the data, which is thought to be a rarefaction wave. The comparison between the experimental absorption data and the fitted model allows for an assessment of the model's accuracy and its ability to capture the observed absorption trends.

Upon examining the plots, a notable trend becomes evident: as the temperature increases within each shock group, the formation of iodine also intensifies, and the rise becomes steeper. This observation suggests a correlation between temperature and iodine formation in the thermal dissociation of C_2H_5I .

These findings align with the expected behavior based on the underlying reaction kinetics. Higher temperatures typically provide more energy for molecular dissociation, leading to enhanced reaction rates and, in this case, increased iodine formation.

From the plots, a particular region of the data stands out because of its unsatisfactory fit: this region corresponds to the formation of the stagnation bubble inside the shock tube, which has a feature of a valley in the absorption signal around 0.05 ms. To ensure a more accurate analysis, the period from the formation of the stagnation bubble to the arrival of the reflected shock was selected to be analyzed.

The decision to focus on this specific range is driven by the fact that the formation of the stagnation bubble introduces uncertainties into the data: by excluding this region from the fitting analysis, potential deviations caused by this phenomenon can be eliminated. Figure 25 illustrates the curve fitting analysis for the same two experiment groups, within these two points.

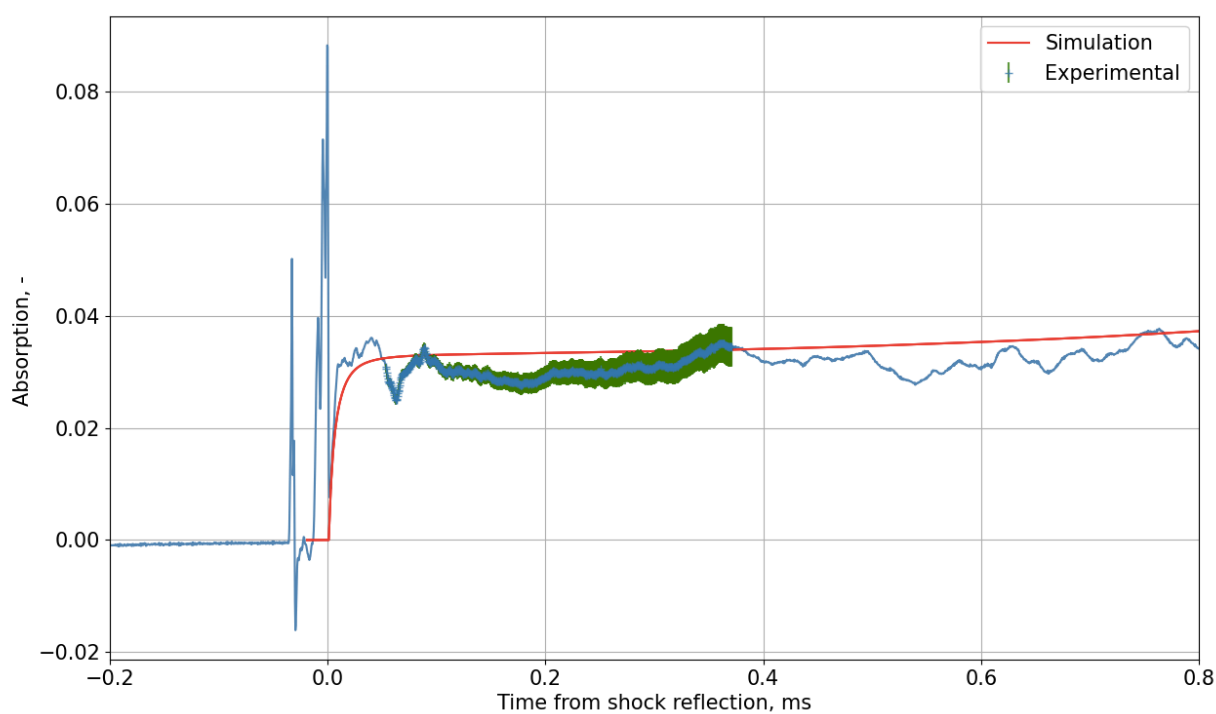
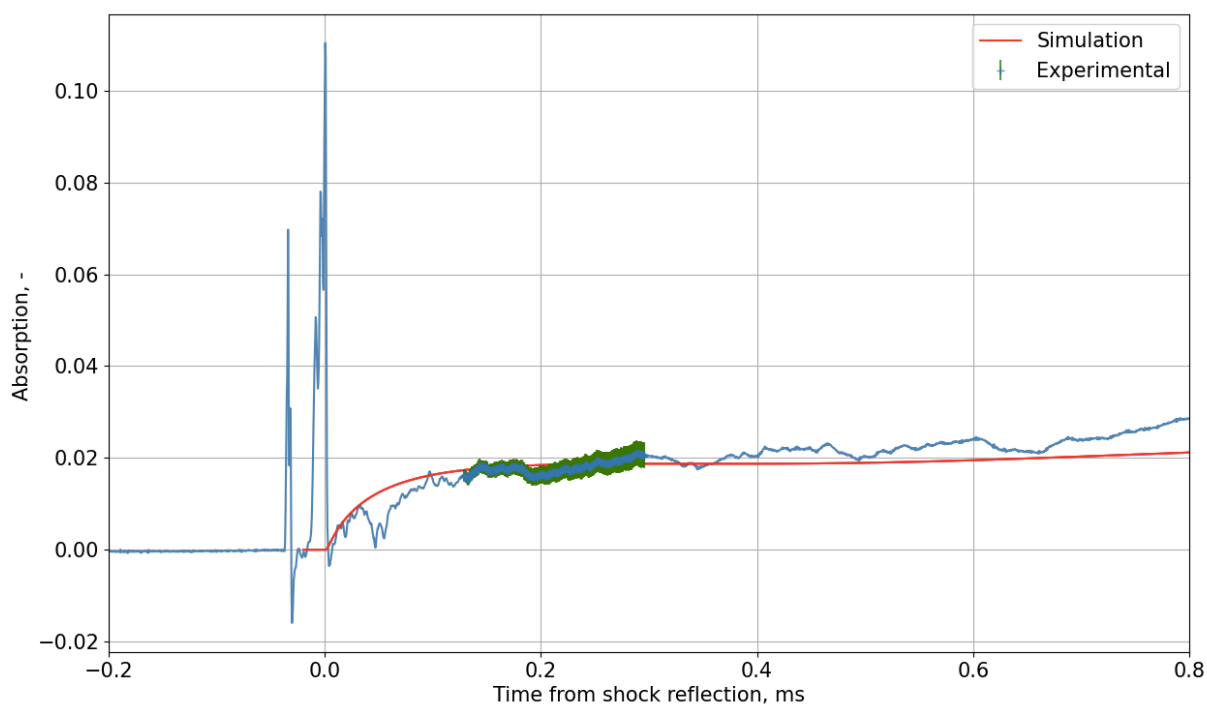


Figure 25: Curve fitting analysis for two temperature ranges (1137-1198 K on top and 1401-1495 K on bottom) focusing on the period from stagnation bubble formation to reflected wave arrival.

Given the evident improvement in the fitting analysis observed in Figure 25, it is reasonable to utilize this specific portion of the data to define the rate constant for C_2H_5I 's thermal dissociation.

The closer agreement between the simulated curve and the experimental data in this region suggests that it provides a more accurate representation of the dissociation kinetics. To enhance the fitting between the simulated and experimental data, an adjustment was made to the absorption cross-section value multiplying it by a factor of 0.8. This adjustment considers potential discrepancies in the absorption cross-section modeled, accounting a 20% uncertainty value.

allowing the absorbance values to float can be a more appropriate approach.

The shape of the absorption curve can provide critical information about reaction kinetics. In such cases, slight variations in the absolute absorbance values may not significantly impact the overall analysis and interpretation of the data. Instead, the main objective is to capture the overall trend and behavior of the absorption profiles across different experiments. By allowing the absorbance values to float within a reasonable range, better overall fit and alignment of the absorption profiles can be achieved, enhancing the comparability and reliability of the data. This approach acknowledges that small variations in experimental conditions or measurement techniques can result in slight differences in the absolute absorbance values, but the overall shape of the absorption profiles remain more meaningful for the rate constant trend.

In the course of conducting experiments with C_2H_5I , an unexpected observation of soot formation was made. Soot, which is formed as a byproduct of incomplete combustion, represents the presence of carbon particles and can significantly impact experimental conditions and signal measurements due to its residuals on the shock tube windows. A notable variation in the signals obtained from one experimental day to another was observed, indicating its influence of on the experimental outcomes, as shown in Figure 26.

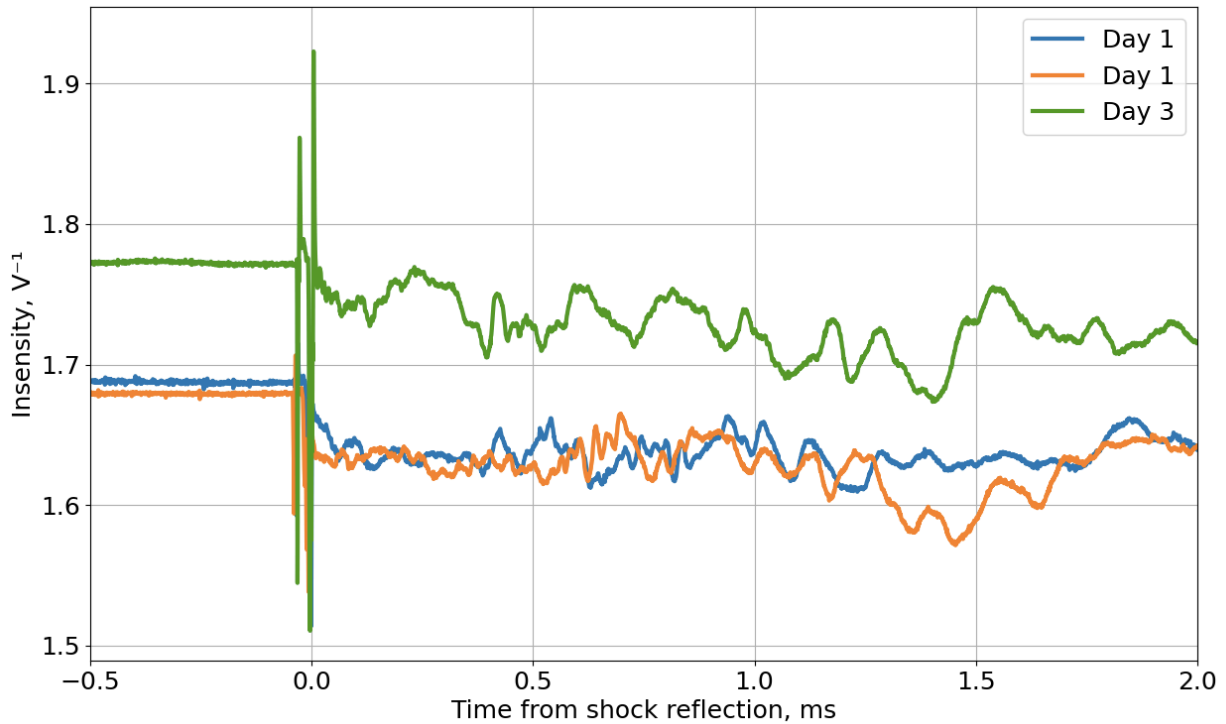


Figure 26: Comparison of three experiments, two ran on the first day and one on the third, with 1% C_2H_5I at $T=1375$ K.

The two signals from the same day are not significantly different, while the signal from the third day is much higher. To ensure consistency and minimize the impact of soot formation, the analysis for this system focused solely on the experiments conducted on the first day. By narrowing the scope to a single day, the study aimed to reduce potential confounding factors, enabling a more controlled analysis and a clearer interpretation of the experimental results. This approach ensures that any observed trends and conclusions drawn are more reliable and directly attributed to the effects of C_2H_5I rather than external variations in experimental conditions. Therefore, only the 300 experiments ran on the first day were considered. The resulting binned groups are shown in Figure 27.

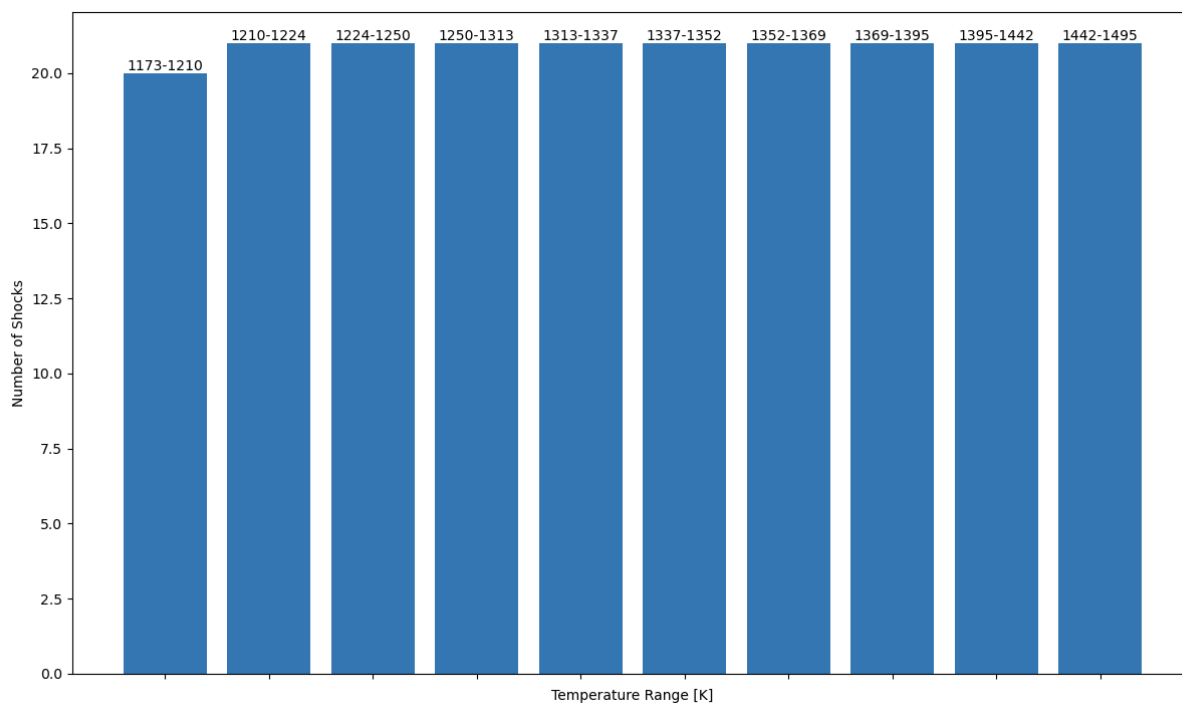


Figure 27: Shocks distribution for each group and its temperature range in C_2H_5I experiments from one day.

By using the parameters obtained from the fitting process for all the sets of binned experiments, it becomes possible to generate an Arrhenius plot, shown in Figure 28.

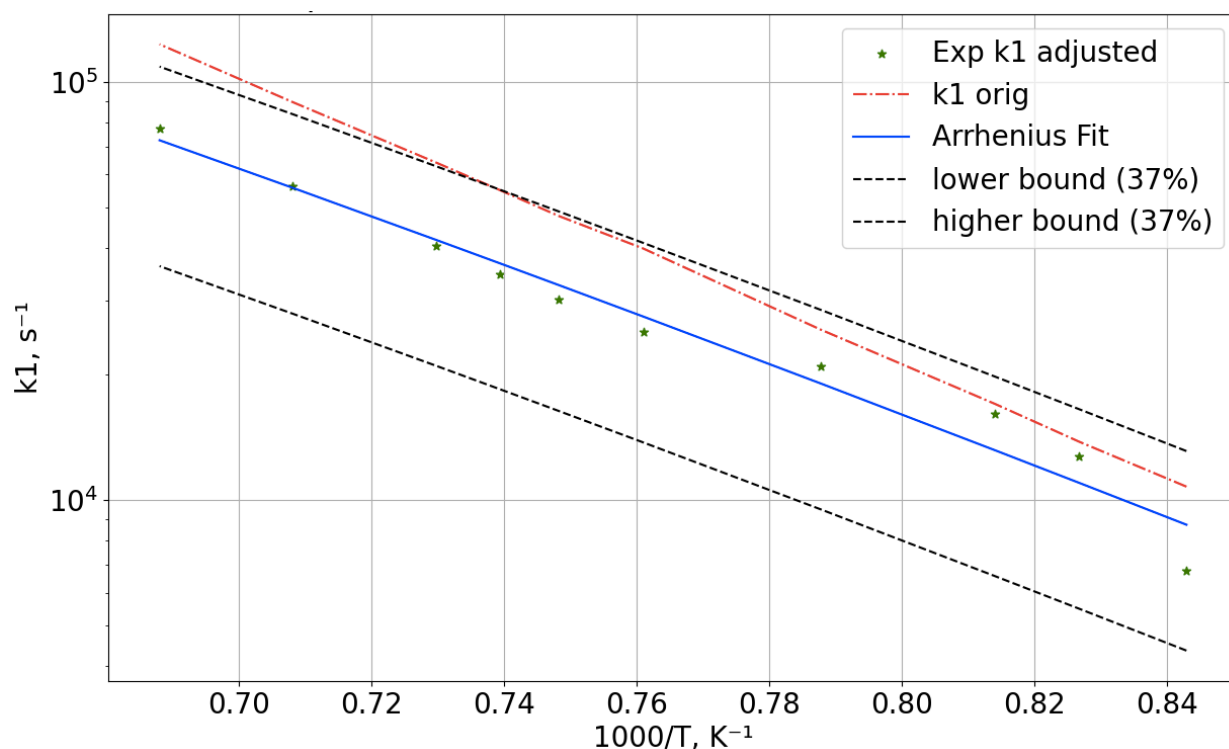


Figure 28: Arrhenius plot comparing experimentally determined rate constant (blue line) with the uncertainty limits (black dashed lines) and the rate constant from the mechanism file (red line) for $\text{C}_2\text{H}_5\text{I}$ experiments.

The green stars on Figure 28 represent the rate constant values obtained through the curve fitting analysis. These points indicate the experimentally determined rate constants at various temperature points, one for each group of binned experiments. The blue line represents the curve fitted through these points, which represents the averaged rate constant value derived from the analysis. The black dashed lines represent the range of uncertainty, with a margin of plus or minus 37% around the experimentally determined rate constant values, which is the uncertainty value provided by Bystrov [9].

In addition to the experimental rate constant points, the Arrhenius plot incorporates a red line representing the rate constant from the mechanism file used for the simulation. This rate constant

value serves as a reference or baseline and allows for a comparison between the experimental results and the predicted values.

The outcome of this experimental investigation was the validation of the expected trends and properties associated with the thermal dissociation of C_2H_5I . The measured rate constants aligned well with established literature values at lower temperatures and have a bigger deviation at higher temperatures. This might be due to the effect of secondary reactions that, at higher temperatures, become more relevant and change the accuracy of the model. Another possible reason for the deviation is that soot formation is more relevant at higher temperatures, causing a lowering of the rate constant value.

This validation ensures confidence in the obtained results and serves as a foundation for CF_3I analysis at lower temperatures.

5.4 CF_3I experiments

For the CF_3I analysis, a total of 1296 experiments was run. To be consistent with the C_2H_5I analysis, the absorption cross section was again multiplied by 0.9. Initially, the simulation analysis began by utilizing Cobos et al. [10] rate constant, which was derived from the mechanism file provided by Papas [11]. However, as the analysis progressed and a comparison with the experimental data was made, it became apparent that the fit obtained with the rate constant provided by Cobos was not as satisfactory.

Recognizing the need for a more accurate representation of CF_3I 's thermal dissociation kinetics, the first order rate constant provided by Bystrov et al. [9] was used, which showed improved fitting results compared to the previous one, as shown in Figure 29.

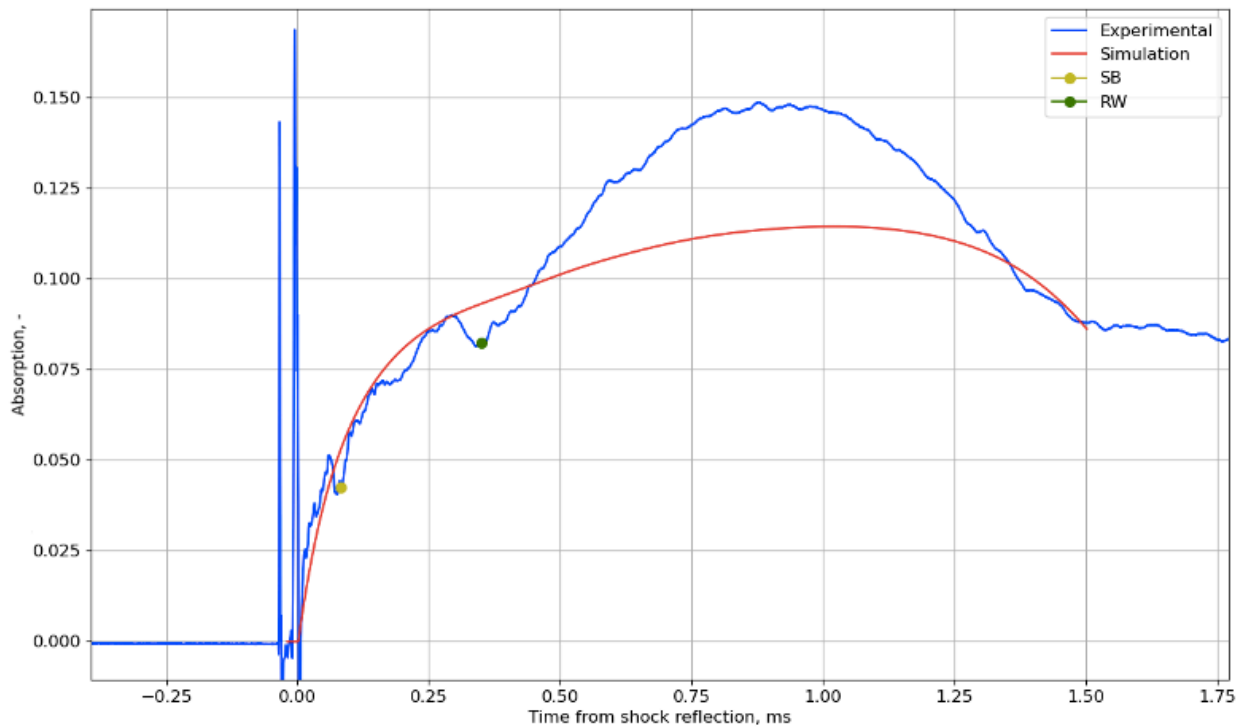
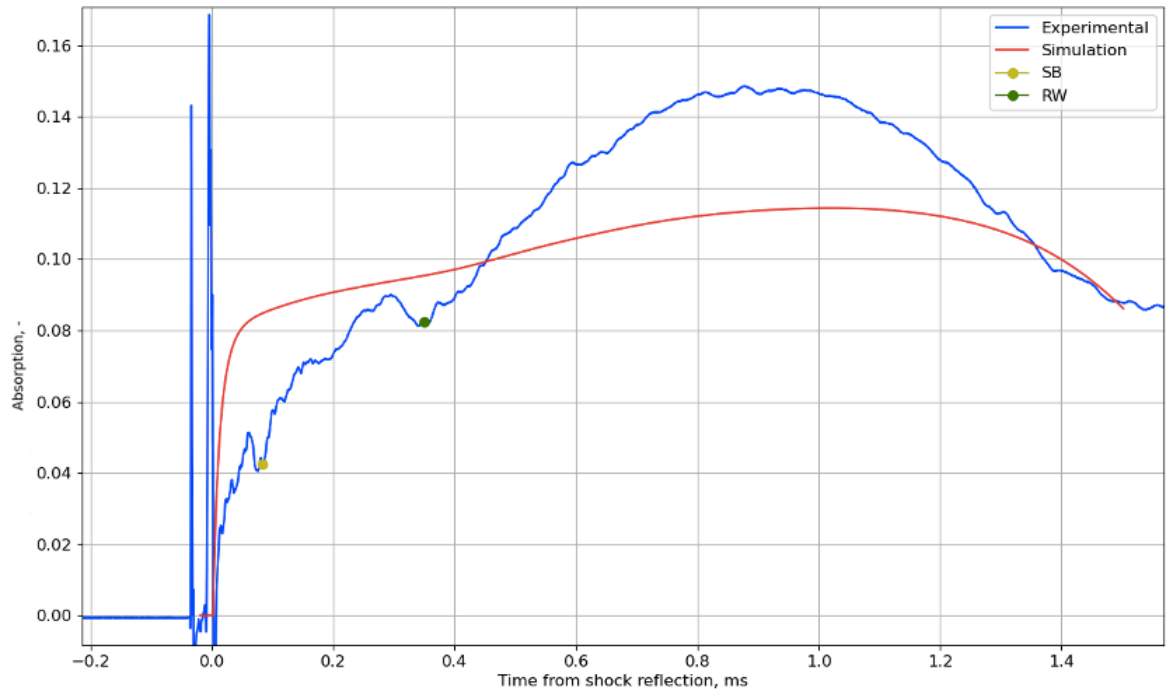


Figure 29: Difference between the agreement between experimental values and simulation curve using the rate constant provided by Cobos et al. [10] (top) and the one by Bystrov et al. [9] (bottom) for one binned group of experiments.

By transitioning from Cobos's [10] rate constant to Bystrov's [9] rate constant, the analysis aimed to optimize the simulation and align it more closely with the experimental observations.

The new mechanism is shown in Table 6.

Table 6: Relevant reactions in the early stages of CF_3I thermal dissociation mechanism.

	Reaction	A	n	E_a	$\Delta H_{r,298K}$	Ref
R1	$CF_3I \rightarrow CF_3 + I$	8.440E11	0.00	4.589E4	54552	[9]
R2	$CF_3 + CF_3 (+M) \rightarrow C_2F_6 + (M)$	k_∞ 9.690E10	0.77	0.00	-99359	[11]
		k_0 1.491E60	-12.51	5.908E3		[11]
R3	$I + I + M \rightarrow I_2 + M$	2.361E14	0.00	-1.500E3	-36114	[11]
R4	$I + CF_3I \rightarrow I_2 + CF_3$	7.590E12	0.00	1.888E4	18438	[11]

The rate constant is expressed as in Equation 7, and the units of the terms in the table are given in cm^3, mol, s, cal .

The result of the fitting is shown in Figure 30, for two sets of binned experiments: the first shock group corresponds to the lowest T5 values (1010-1121 K), while the second group corresponds to the highest T5 values (1426-1526 K).

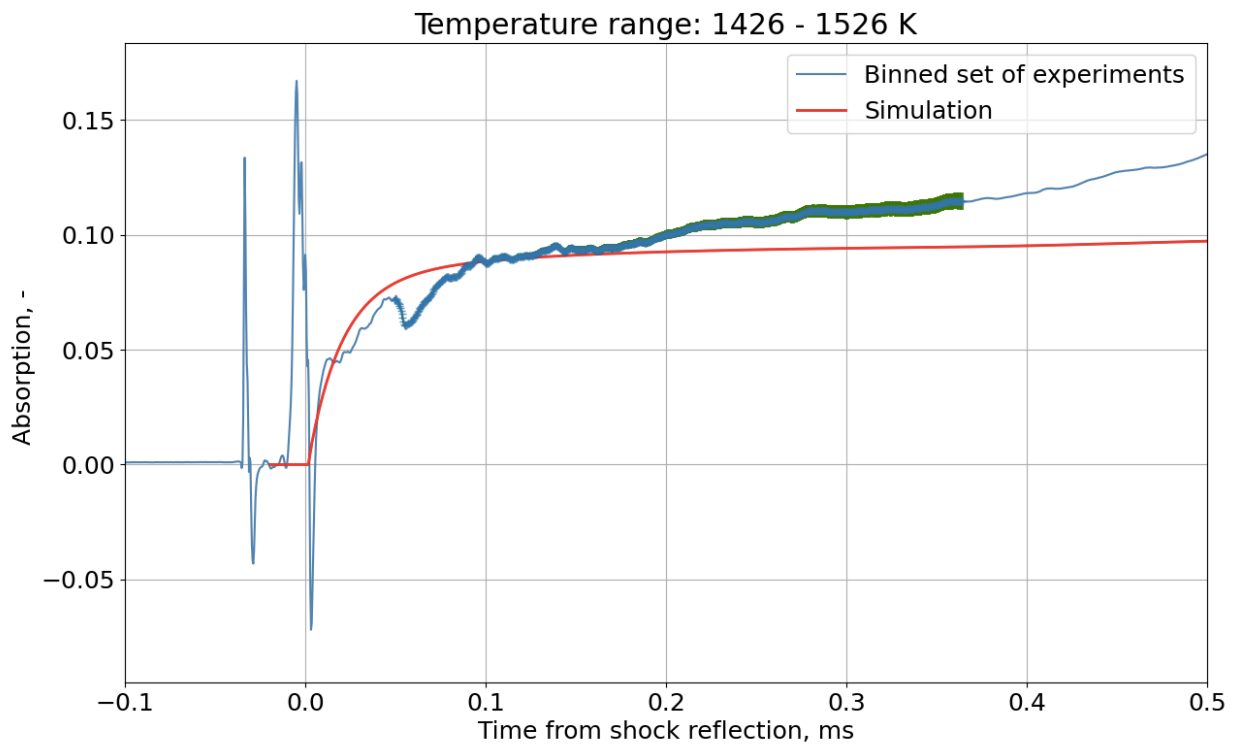
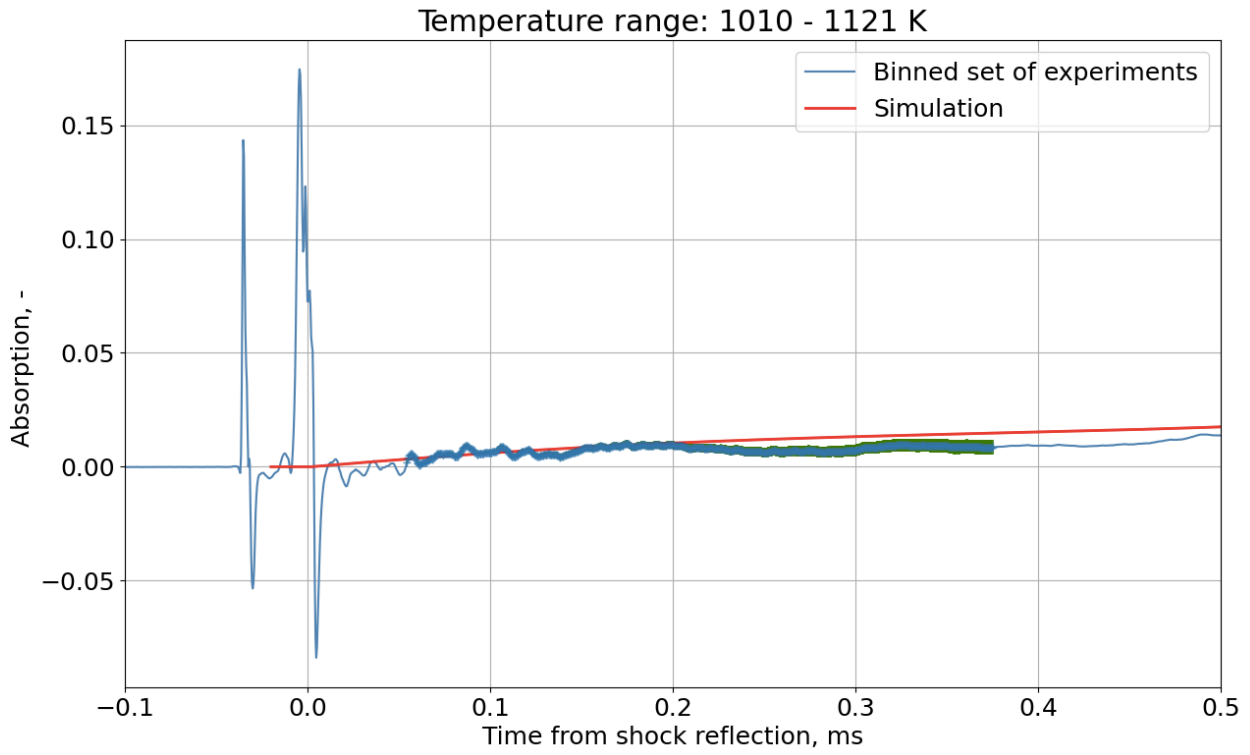
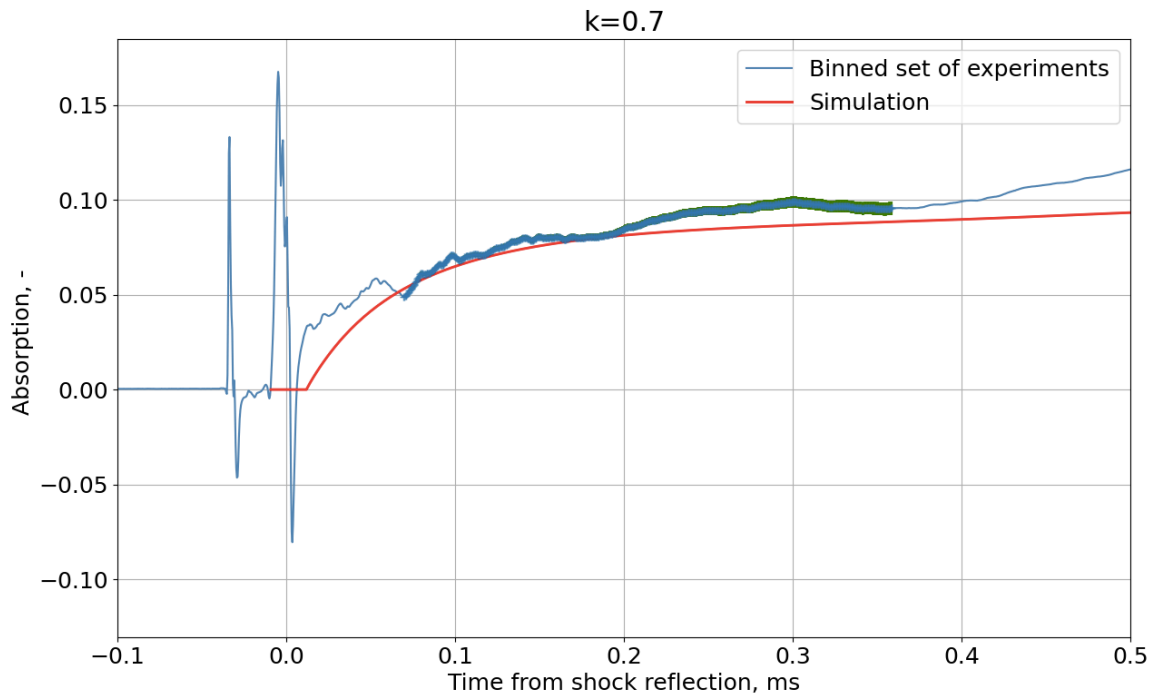


Figure 30: Curve fitting analysis stagnation bubble to rarefaction wave for a low temperature range group of experiments (top) and a high one (bottom).

Figure 30 depicts the curve fitting analysis conducted from the two valleys found in the absorption signal.

Figure 31 shows the result of the fitting process over one set of binned experiments (1309 – 1334 K) using three different values for the coefficient for which the rate constant was multiplied, the first one is 0.7, the second one is the best fit, which is equal to 0.9, and the third one is 1.3.



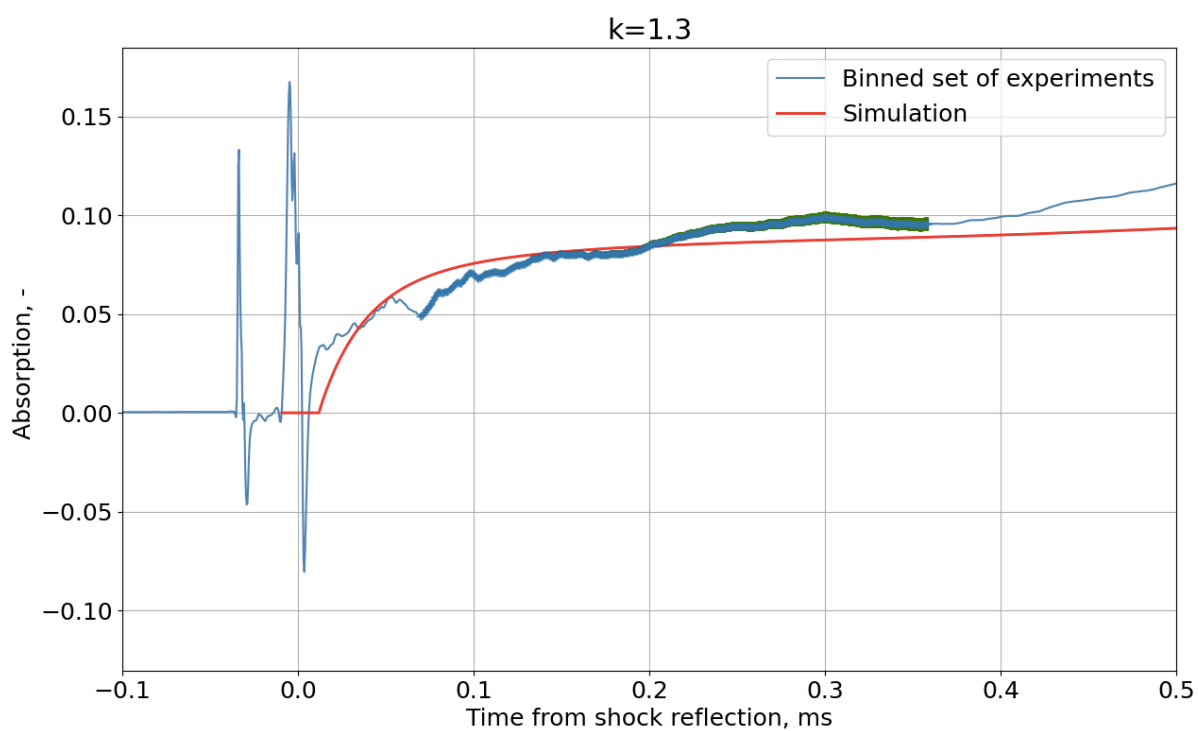
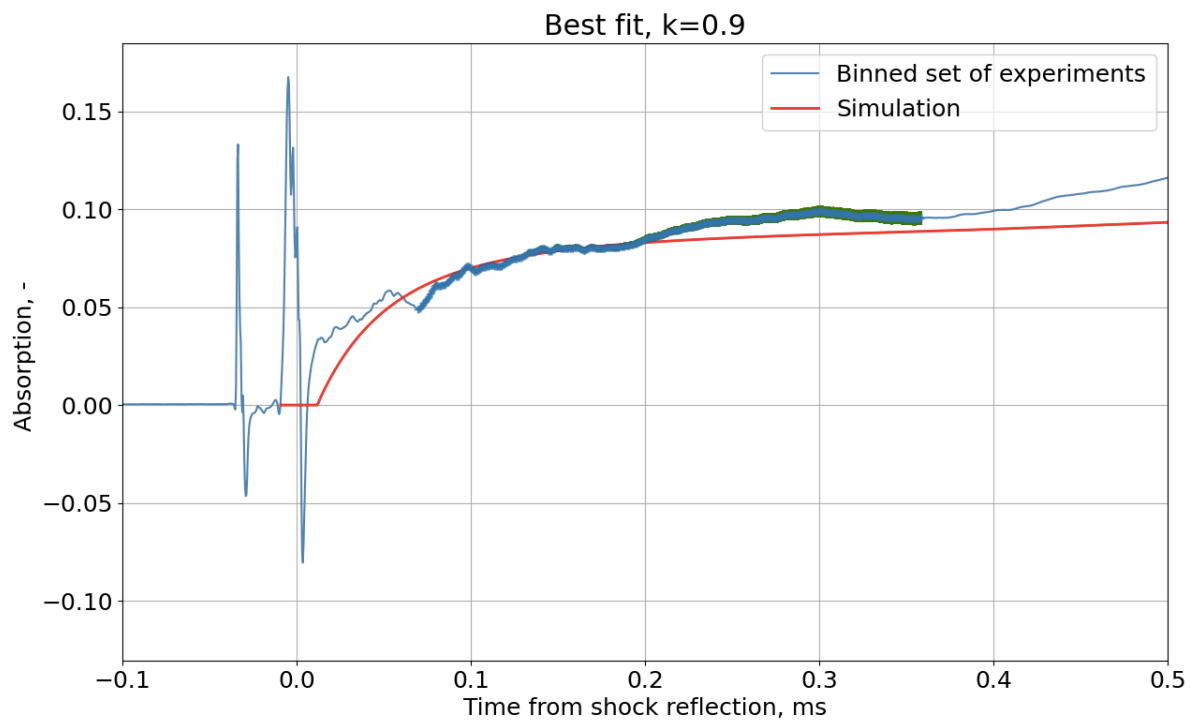


Figure 31: Comparison between different fittings with different coefficients to which the rate constant is multiplied: 0.7, 0.9 (best), 1.3.

As it can be seen from Figure 31, the best fit minimizes the error between the simulation and the experimental results.

The rate constant obtained with this fitting technique is shown in Figure 32.

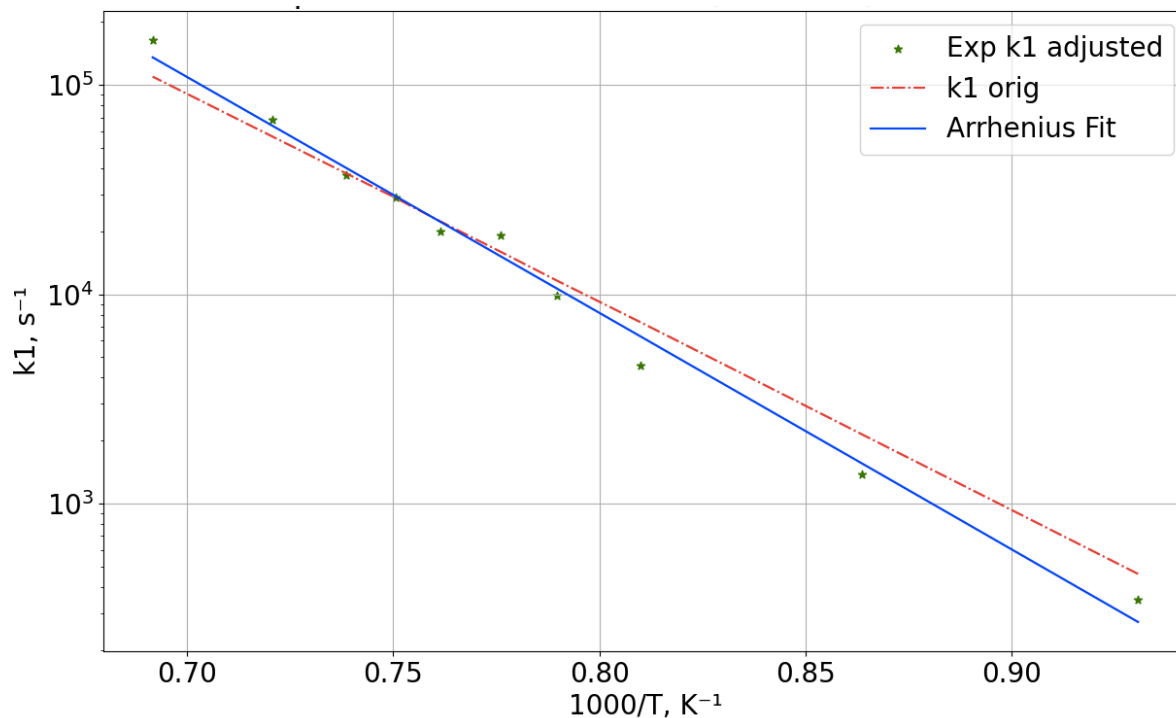


Figure 32: Arrhenius plot comparing experimentally determined rate constant (blue line) with the rate constant from the mechanism file (red dashed line) for CF₃I experiments.

The rate constant obtained from the improved fitting analysis, as shown in Figure 32, well matches with the rate constant from the mechanism file.

The average value of the reaction rate constant obtained over the temperature range is described in Equation 20:

$$k(T) = 10^{14.61} \cdot T^{-0.47} \cdot \exp\left(-\frac{11132}{T}\right) \quad [s^{-1}]. \quad (20)$$

Figure 33 shows the rate constant found in this work with the rate constants present in literature.

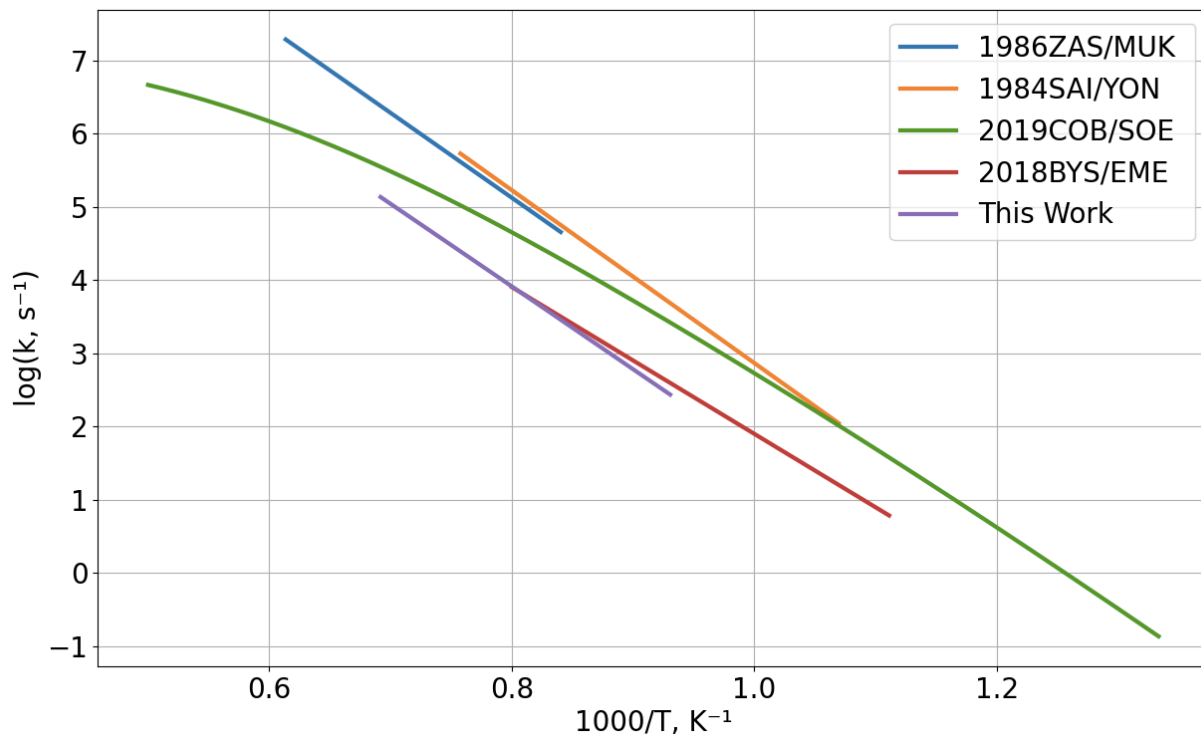


Figure 33: CF_3I thermal dissociation rate constant for different studies and compared to this work.

Figure 34 shows the rate constants found in this work and by Bystrov et al. [9], and compares them with their high-pressure limit rate constant. The rate constants are below the high-pressure limit.

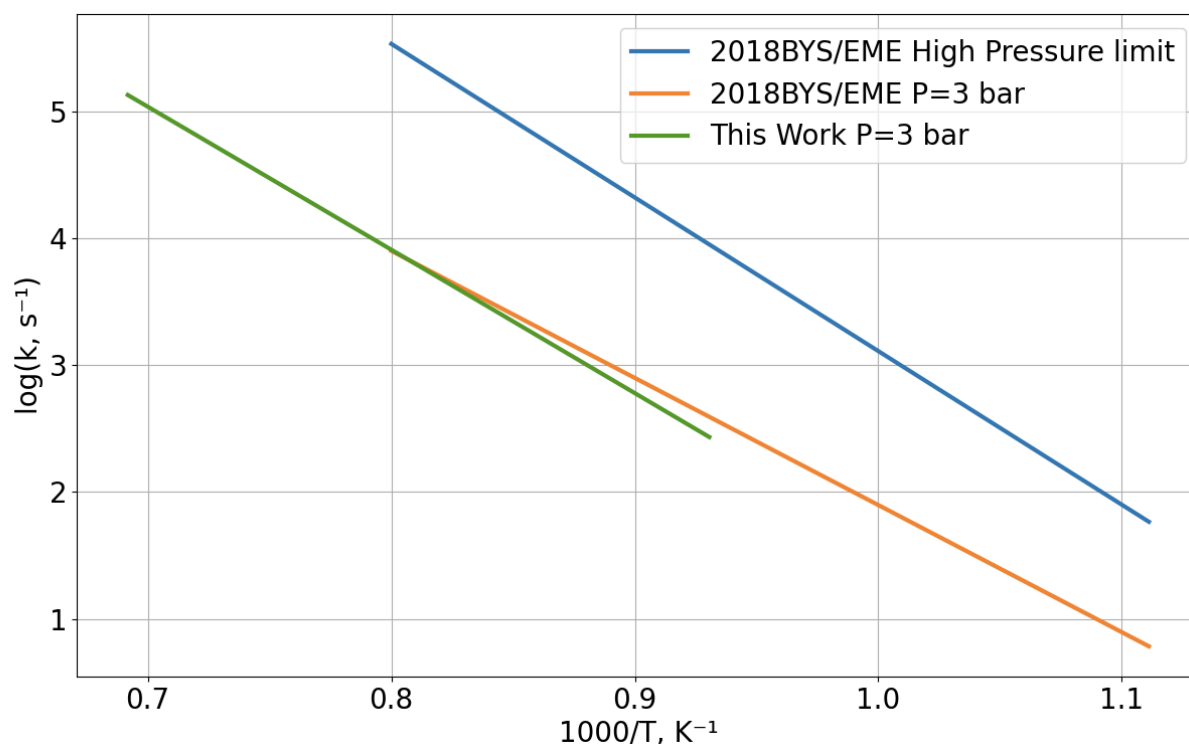


Figure 34: Comparison between first order rate constants and high-pressure limit by Bystrov et al. [9].

The measured rate constant obtained provides valuable information in resolving the discrepancy in the rate constants reported in the literature. The agreement of the measured rate constant with Bystrov's rate constant at 3 bar suggests that the experimental data aligns closely with Bystrov's findings. Furthermore, the observation that the measured rate constant is within the close range of Cobos' high-pressure limit rate constant at 3 bar further supports the reliability and accuracy of the measurements.

By obtaining a rate constant that is in reasonable agreement with established values and addressing the discrepancies in the literature, these findings contribute to a better understanding of the reaction kinetics and provide important insights into the reaction mechanism under the specified conditions.

6. Conclusions and Recommendations for Future Work

This study had one main scope: the determination of the thermal dissociation rate constant of CF_3I , a potential fire suppressant with the identification of a reliable experimental and analysis method for shock tube studies to overcome the challenges related to a low signal strength.

By conducting experiments in a controlled environment using a shock tube, the rate constant was measured, providing a value for CF_3I 's rate constant over the temperature range of 1000 K to 1500 K.

In addressing the challenge of low signal strength during the analysis of CF_3I 's thermal dissociation, various experimental techniques were employed to optimize the data acquisition process. Fixed wavelength single pass and fixed wavelength double pass measurements were conducted. Fixed wavelength single pass approach provided some insights, the low signal strength posed limitations in accurately quantifying the kinetics for the thermal dissociation reaction. To overcome this limitation, double pass measurements were implemented. The double pass method effectively reduced the signal-to-noise ratio, enhancing the overall quality of the acquired data. By increasing the signal strength and reducing noise, the precision and reliability of the measurements were significantly improved. By employing the double pass technique, the accuracy in the analysis of CF_3I 's thermal dissociation kinetics improved.

To analyze the experiments a robust processing model was created. The data processing techniques employed in this study included the exclusion of inadequate experiments, binning of experiments, alignment and averaging of pressure signals, identification of the peculiar points of the experiments and the fitting of the rate constant through an iterative process. These techniques

allowed for the determination of the most accurate rate constant value that described the thermal dissociation kinetics of CF_3I .

The implementation of double pass measurements proved to be instrumental in overcoming the challenges posed by low signal strength during the analysis of CF_3I 's thermal dissociation. This technique effectively reduced the signal-to-noise ratio, and enhanced the precision of the measurements. By optimizing the data acquisition process, the study achieved more reliable and accurate results, further enhancing our understanding of CF_3I 's thermal dissociation kinetics and reactivity.

The significance of experimental validation cannot be overstated, as the obtained results contribute to the existing knowledge base on CF_3I 's reactivity. Experimental validation is crucial to ensuring the reliable and safe implementation of CF_3I as a fire suppressant in real-world fire safety applications.

In summary, this study has advanced our understanding of CF_3I 's thermal dissociation kinetics and reactivity, providing valuable data for further analysis and comparison with theoretical models. The findings have practical implications in the field of fire suppression, supporting the development of more efficient and environmentally friendly fire suppression systems. Future research efforts should focus on addressing the remaining uncertainties and optimizing the utilization of CF_3I for enhanced fire safety.

References

- [1] R. G. Gann, “NGP Final Report,” *NIST*, Dec. 2011, Accessed: Jul. 06, 2023. [Online]. Available: <https://www.nist.gov/el/fire-research-division-73300/product-services/next-generation-fire-suppression-technology/ngp>
- [2] Page, “Stratospheric Ozone Protection: 30 Years of Progress and Achievements,” 2017. Available: https://www.epa.gov/sites/default/files/2017-12/documents/mp30_report_final_508v3.pdf
- [3] “Scientific Assessment of ozone Depletion: 2010 Pursuant to Article 6 of the Montreal Protocol on Substances that Deplete the Ozone Layer National Oceanic and Atmospheric Administration National Aeronautics and Space Administration United Nations Environment Programme World Meteorological Organization European Commission.” Available: <https://ozone.unep.org/sites/default/files/2019-05/00-SAP-2010-Assement-report.pdf>
- [4] M. Ko, P. Newman, S. Reimann, and S. Strahan, “Recommended values Atmospheric Lifetimes for CFC-11 and CFC-12 CFC-11 Lifetimes of Stratospheric Ozone-Depleting Substances, Their Replacements, and Related Species,” 1990. Accessed: Jun. 22, 2023. [Online]. Available: https://www.sparc-climate.org/fileadmin/customer/6_Publications/SPARC_reports_PDF/6_SPARC_LifetimeReport_Web.pdf
- [5] D. A. Knyazkov, T. A. Bolshova, V. M. Shvartsberg, I. E. Gerasimov, A. G. Shmakov, and O. P. Korobeinichev, “Effect of inhibitors on flammability limits of dimethyl ether/air mixtures,” *Proceedings of the Combustion Institute*, vol. 37, no. 3, pp. 4267–4275, 2019, doi: <https://doi.org/10.1016/j.proci.2018.06.109>.
- [6] “NIST Chemical Kinetics Database,” *kinetics.nist.gov*. <https://kinetics.nist.gov/kinetics/Search.jsp> (accessed Jun. 22, 2023).
- [7] I. S. Zaslanko, Yu. K. Mukoseev, G. A. Skorobogatov, and V. K. Khripun, “Measurement of the rate constant for the thermal dissociation of gaseous CF₃I,” *in a shock tube Kinet. Catal.* 31 912–8, 1990.
- [8] K. Saito, Y. Yoneda, H. Tahara, S. Kidoguchi, and I. Murakami, “The Thermal Decomposition of CF₃I in Ar,” vol. 57, no. 9, pp. 2661–2662, Sep. 1984, doi: <https://doi.org/10.1246/bcsj.57.2661>.
- [9] N. S. Bystrov, A. V. Emelianov, A. V. Eremin, and P. I. Yatsenko, “Direct measurements of rate coefficients for thermal decomposition of CF₃I using shock—tube ARAS technique,” *Journal of Physics D: Applied Physics*, vol. 51, no. 18, p. 184004, Apr. 2018, doi: <https://doi.org/10.1088/1361-6463/aab8e5>.

- [10] C. J. Cobos, L. Sölter, E. Tellbach, and J. Troe, “Falloff curves and mechanism of thermal decomposition of CF_3I in shock waves,” *Physical Chemistry Chemical Physics*, vol. 21, no. 43, pp. 23893–23899, 2019, doi: <https://doi.org/10.1039/c9cp04771a>.
- [11] P. Papas, C. Cao, W. Kim, E. Baldwin, and A. Chattaway, “Fire suppression using trifluoroiodomethane (CF_3I)-carbon dioxide (CO_2) mixtures,” *Proceedings of the Combustion Institute*, vol. 39, no. 3, pp. 3765–3773, Jan. 2023, doi: <https://doi.org/10.1016/j.proci.2022.07.257>.
- [12] “Cantera,” *cantera.org*. <https://cantera.org/>
- [13] S. R. Turns, *An introduction to combustion : concepts and applications*. New York: McGraw-Hill, 2012.
- [14] “Burcat’s Thermodynamic Data,” *garfield.chem.elte.hu*. <http://garfield.chem.elte.hu/Burcat/burcat.html> (accessed Jun. 22, 2023).
- [15] X. Yang and R. S. Tranter, “High-temperature dissociation of ethyl radicals and ethyl iodide,” *International Journal of Chemical Kinetics*, vol. 44, no. 7, pp. 433–443, Jan. 2012, doi: <https://doi.org/10.1002/kin.20601>.
- [16] S. S. Kumaran, M.-C. . Su, K. P. Lim, and J. V. Michael, “The thermal decomposition of $\text{C}_2\text{H}_5\text{I}$,” *Symposium (International) on Combustion*, vol. 26, no. 1, pp. 605–611, Jan. 1996, doi: [https://doi.org/10.1016/s0082-0784\(96\)80266-9](https://doi.org/10.1016/s0082-0784(96)80266-9).
- [17] H. Wang, X. You, A.V. Joshi, S.G. Davis, A. Laskin, F. Egolfopoulos & C.K. Law, USC Mech Version II. High-Temperature Combustion Reaction Model of $\text{H}_2/\text{CO}/\text{C}_1\text{-C}_4$ Compounds. http://ignis.usc.edu/USC_Mech_II.htm, May 2007.”
- [18] P. T. Lynch, “Note: An improved solenoid driver valve for miniature shock tubes,” *Review of Scientific Instruments*, vol. 87, no. 5, p. 056110, May 2016, doi: <https://doi.org/10.1063/1.4953115>.
- [19] S. Janardhanraj, S. K. Karthick, and A. Farooq, “A review of diaphragmless shock tubes for interdisciplinary applications,” *Progress in Energy and Combustion Science*, vol. 93, p. 101042, Nov. 2022, doi: <https://doi.org/10.1016/j.pecs.2022.101042>.
- [20] R. S. Tranter and P. T. Lynch, “A miniature high repetition rate shock tube,” *The Review of Scientific Instruments*, vol. 84, no. 9, p. 094102, Sep. 2013, doi: <https://doi.org/10.1063/1.4820917>.
- [21] P. T. Lynch and G. Wang, “Chemical thermometry in miniature HRRST using 1,1,1-trifluoroethane dissociation,” *Proceedings of the Combustion Institute*, vol. 36, no. 1, pp. 307–314, Jan. 2017, doi: <https://doi.org/10.1016/j.proci.2016.05.057>.

- [22] S. Li, W. Ren, D. B. Davidson, and R. K. Hanson, "Boundary Layer Effects behind Incident and Reflected Shock Waves in a Shock Tube," pp. 471–476, Jan. 2012, doi: https://doi.org/10.1007/978-3-642-25685-1_71.
- [23] R. A. Shaik, A. L. Kastengren, R. S. Tranter, and P. T. Lynch, "Temporally and spatially resolved X-ray densitometry in a shock tube," *Combustion and Flame*, vol. 224, pp. 136–149, Feb. 2021, doi: <https://doi.org/10.1016/j.combustflame.2020.09.035>.
- [24] C. M. Murzyn, "Diode laser gas sensing for high-speed temperature and speciation measurements inside explosive fireballs," *www.ideals.illinois.edu*, Oct. 17, 2018. <https://hdl.handle.net/2142/102898> (accessed Jun. 22, 2023).
- [25] R. Hanson, R Mitchell Spearrin, and C. S. Goldenstein, *Spectroscopy and optical diagnostics for gases*. Cham, Switzerland: Springer, 2016.
- [26] E. L. Petersen and R. K. Hanson, "Measurement of Reflected-shock Bifurcation Over a Wide Range of Gas Composition and Pressure," *Shock Waves*, vol. 15, no. 5, pp. 333–340, Sep. 2006, doi: <https://doi.org/10.1007/s00193-006-0032-3>.
- [27] R. A. Shaik, R. Sivaramakrishnan, A. J. Jasper, R. S. Tranter, and P. T. Lynch, "A Study on Initial Decomposition of Difluoromethane (CH₂F₂) Using Laser Absorption Spectroscopy in a Miniature Shock Tube," in USNMC 2023 College Park TX."T